

1           **Shear-driven formation of olivine veins by dehydration of ductile**  
2           **serpentinite: a numerical study with implications for transient weakening**

3           **Stefan M. Schmalholz<sup>1</sup>, Evangelos Moulas<sup>2</sup>, Ludovic Räss<sup>3,4</sup> and Othmar Müntener<sup>1</sup>**

4           <sup>1</sup>Institute of Earth Sciences, University of Lausanne, 1015 Lausanne, Switzerland

5           <sup>2</sup>Institut of Geosciences and Mainz Institute of Multiscale Modeling (M<sup>3</sup>ODEL), Johannes  
6           Gutenberg University of Mainz, Germany

7           <sup>3</sup>Laboratory of Hydraulics, Hydrology and Glaciology (VAW), ETH Zurich, Zurich,  
8           Switzerland

9           <sup>4</sup>Swiss Federal Institute for Forest, Snow and Landscape Research (WSL), Birmensdorf,  
10           Switzerland

11           Email, corresponding author: Stefan Schmalholz ([stefan.schmalholz@unil.ch](mailto:stefan.schmalholz@unil.ch))

12           Evangelos Moulas: [evmoulas@uni-mainz.de](mailto:evmoulas@uni-mainz.de); Ludovic Räss: [luraess@ethz.ch](mailto:luraess@ethz.ch);

13           Othmar Müntener: [Othmar.Muntener@unil.ch](mailto:Othmar.Muntener@unil.ch)

14  
15           **Key points:**

- 16           • During viscous simple-shearing of serpentinite, en-échelon olivine veins form by  
17           dehydration and grow in direction parallel to compression
- 18           • Vein formation is a self-limiting process and kinetic reaction rate must be faster than  
19           fluid-pressure diffusion rate to form olivine
- 20           • Porosity evolution is controlled by three mechanisms: volume change, temporal solid  
21           density variation and reactive mass transfer

22 **Abstract**

23 Serpentinite subduction and the associated formation of dehydration veins is important for  
24 subduction zone dynamics and water cycling. Field observations suggest that en-échelon  
25 olivine veins in serpentinite mylonites formed by dehydration during simultaneous shearing of  
26 ductile serpentinite. Here, we test a hypothesis of shear-driven formation of dehydration veins  
27 with a two-dimensional hydro-mechanical-chemical numerical model. We consider the  
28 reaction antigorite + brucite = forsterite + water. Shearing is viscous and the shear viscosity  
29 decreases exponentially with porosity. The total and fluid pressures are initially homogeneous  
30 and in the antigorite stability field. Initial perturbations in porosity, and hence viscosity, cause  
31 fluid pressure perturbations. Dehydration nucleates where the fluid pressure decreases locally  
32 below the thermodynamic pressure defining the reaction boundary. Dehydration veins grow  
33 during progressive simple-shearing in a direction parallel to the maximum principal stress,  
34 without involving fracturing. The porosity evolution associated with dehydration reactions is  
35 controlled to approximately equal parts by three mechanisms: volumetric deformation, solid  
36 density variation and reactive mass transfer. The temporal evolution of dehydration veins is  
37 controlled by three characteristic time scales for shearing, mineral-reaction kinetics and fluid-  
38 pressure diffusion. The modelled vein formation is self-limiting and slows down due to fluid  
39 flow decreasing fluid pressure gradients. Mineral-reaction kinetics must be significantly faster  
40 than fluid-pressure diffusion to generate forsterite during vein formation. The self-limiting  
41 feature can explain the natural observation of many, small olivine veins and the absence of  
42 few, large veins. We further discuss implications for transient weakening during  
43 metamorphism and episodic tremor and slow-slip in subduction zones.

44

45

46 **Plain language summary**

47 Serpentinite is a rock that contains water which is bound within the crystal lattice. When  
48 serpentinite is plunging together with tectonic plates into the Earth mantle, the changing  
49 pressure and temperature conditions cause chemical reactions which releases the water bound  
50 in the crystal lattice; a process called dehydration. A typical mineral that forms by  
51 dehydration is olivine. Dehydration is important for the global water cycle, since much water  
52 is transferred with tectonic plates into the mantle and is migrating back to the Earth surface  
53 after dehydration. However, many aspects of the water cycle remain still unclear, since  
54 dehydration during plunging of tectonic plates involves the incompletely understood  
55 interaction of three fundamental mechanical and chemical processes: mechanical deformation  
56 of the rock, porous flow of released fluid and chemical reactions involving changes in rock  
57 density. Here, we present a new mathematical model to investigate the coupled processes of  
58 rock deformation, fluid flow and dehydration reactions. We present computer simulations  
59 which can explain why the dehydration occurs in narrow and elongated regions which are  
60 termed veins. We propose that our simulations could explain the observation of many small  
61 olivine veins in strongly sheared serpentinite.

62

## 63 1. Introduction

64 The dehydration of serpentinite at subduction zones is an important process for the  
65 global water cycle (e.g., Peacock, 1990; Pettke and Bretscher, 2022; Ulmer and Trommsdorff,  
66 1995; Rupke et al., 2004), for the dynamics and seismicity at subduction zones (e.g., Bloch et  
67 al., 2018; Hacker et al., 2003) or for arc magmatism due to hydration of the mantle wedge  
68 (e.g., Hebert et al., 2009; John et al., 2012). More generally, the interaction of mineral  
69 reactions, fluid flow and rock deformation is important for a variety of geodynamic processes,  
70 such as chemical and volatile cycling (e.g., Bebout, 2014) or reaction-induced weakening of  
71 faults and shear zones (e.g., Labrousse et al., 2010; Sulem and Famin, 2009), as well as for  
72 practical applications such as natural carbon storage (e.g., Matter and Kelemen, 2009) or  
73 geothermal energy exploitation (e.g., Pandey et al., 2018). However, many aspects of the  
74 coupling of mineral reactions, fluid flow and rock deformation are still unclear.

75 Indirect observations that have been attributed to serpentinite dehydration at  
76 subduction zones are aseismic episodic tremor and slow-slip (ETS) phenomena (e.g., Burlini  
77 et al., 2009; Tarling et al. 2019). These phenomena are commonly thought to result from  
78 episodic fault slip, likely facilitated or promoted by pulses of fluid release associated with  
79 fluid pressure variations (e.g., Audet et al., 2009; Connolly, 1997; Frank et al., 2015;  
80 Gomberg et al., 2010; Shelly et al., 2006; Taetz et al., 2018). For example, such slow-slip  
81 occurs on the plate interface in Cascadia at 30 to 40 km depth (e.g., Gomberg et al., 2010) and  
82 for temperatures probably between 400 and 500 °C (e.g., Tarling et al., 2019 and references  
83 therein). However, how the dehydration reaction, the associated fluid release and the  
84 volumetric and shear deformation of the involved rocks are coupled and actually cause the  
85 episodic slow-slip phenomena remains elusive.

86 Direct observation of the dehydration of serpentinite at subduction zones is not  
87 possible in nature. However, field observations in areas with abundant exposed serpentinites

88 at variable pressure and temperature may provide insight into incipient dehydration stages. In  
89 the European Alps, exposed serpentinites, which experienced variable peak pressures and  
90 temperatures, are abundant in many regions. Examples are the serpentinites of Saas Zermatt  
91 (Western Alps) or of the Erro-Tobbio unit (Voltri massif, Ligurian Alps, Italy; e.g., Hermann  
92 et al., 2000; Peters et al., 2020; Plümper et al., 2017; Scambelluri et al. 1991, Scambelluri et  
93 al., 1995; Kempf et al., 2020). These serpentinite bearing regions are key areas that preserve  
94 ductile and brittle structures that are related to fluid release. The serpentinites of the Erro-  
95 Tobbio unit exhibit olivine-bearing veins and the metamorphic olivine most likely results  
96 from the breakdown of antigorite and brucite (Fig. 1; e.g., Hermann et al., 2000; Plümper et  
97 al., 2017; Scambelluri et al., 2004). The olivine veins occur in two settings: as minimally  
98 deformed veins within little deformed, variably serpentinitized peridotite and as deformed  
99 veins within strongly deformed antigorite serpentinite, described as a serpentinite mylonite  
100 (Fig. 1; e.g., Hermann et al., 2000; Plümper et al., 2017). These serpentinite mylonites are cut  
101 by en-échelon olivine veins, which in turn are dissected by multiple sets of olivine-bearing  
102 shear bands (Hermann et al., 2000). Plümper et al. (2017) suggest that the association of  
103 undeformed and sheared veins attests that dehydration-induced vein formation was  
104 synchronous with ductile deformation in the enclosing serpentinite mylonites. Furthermore,  
105 Hermann et al. (2000) hypothesize that (i) multiple sets of olivine shear bands provide  
106 evidence for continuous deformation, (ii) sheared olivine-rich veins are probably very weak  
107 due to continuous solution and precipitation in the presence of a fluid phase, (iii) fluid  
108 produced by the dehydration reaction was (partially) trapped in the serpentinite mylonite and  
109 (iv) serpentinite mylonites are not only zones with highly localized deformation but also  
110 zones of focused fluid flow. However, these coupled physical-chemical hypotheses for olivine  
111 vein formation have not been tested with theoretical models based on the concepts of  
112 continuum mechanics and thermodynamics. Recently, Huber et al. (2022) presented a hydro-

113 chemical (HC) model to study the formation of olivine veins in dehydrating serpentinite.  
114 However, they do not consider any solid-mechanical aspects of olivine vein formation and do,  
115 hence, not consider volumetric or shear deformation of the serpentinite and associated fluid  
116 pressure changes. Therefore, we cannot apply their model to test the coupled physical-  
117 chemical hypothesis of shear-driven olivine vein formation.

118 Here, we test the hydrological, mechanical and chemical feasibility of a hypothesis for  
119 the formation of observed olivine veins in serpentinite mylonites with a new two-dimensional  
120 (2D) hydro-mechanical-chemical (HMC) model. The hypothesis is (Fig. 2): During viscous  
121 shearing of serpentinite, the magnitudes of ambient pressure and temperature were close to  
122 the magnitudes required for triggering the dehydration reaction from serpentinite to olivine  
123 (Fig. 3A). The effective viscosity of serpentinite was spatially variable, for example due to  
124 variable porosity or heterogeneities in mineralogy (Fig. 2A). Weak domains, with lower  
125 viscosity, cause pressure variations in the sheared serpentinite so that the dehydration  
126 reactions are triggered in domains with locally decreased pressure. The dehydration forms  
127 olivine and increases the porosity locally, which in turn increases the size of weak domains,  
128 consisting of an olivine-fluid mixture. The dehydration region forms vein-like structures that  
129 grow in a direction parallel to the maximal compressive stress without any fracturing (Fig. 2A  
130 and B). After fluid has escaped the olivine-rich region, the olivine-rich veins, observable in  
131 the field, have formed (Fig. 2C). We test this hypothesis with a 2D HMC model because such  
132 models are suitable to theoretically study the coupling between chemical reactions, fluid flow  
133 and deformation (e.g., Kolditz et al., 2015; Poulet et al., 2012). Such coupled models have  
134 been applied to study a variety of geodynamic processes, for example, reaction-driven  
135 cracking during serpentinization (e.g., Evans et al., 2020), porosity evolution and clogging  
136 during serpentinization (e.g. Malvoisin et al., 2021), the impact of dehydration on earthquake  
137 nucleation (e.g., Brantut et al., 2011), the impact of shear heating and associated chemical

138 rock decomposition on thrusting (e.g., Poulet et al., 2014) or reactive melt migration (e.g.,  
139 Aharonov et al., 1997; Baltzell et al., 2015; Bessat et al., 2022; Schiemenz et al., 2011). We  
140 apply here an extension of a HMC model that was previously used to model the dehydration  
141 reaction: brucite = periclase + water (Schmalholz et al., 2020). Here, we elaborate this HMC  
142 model and consider a simple MgO-SiO<sub>2</sub>-H<sub>2</sub>O (MSH) system for the reaction: antigorite +  
143 brucite = forsterite + water (Fig. 3). For simplicity, we consider an isothermal system and a  
144 fixed chemical composition so that the reaction antigorite + brucite = forsterite + water is  
145 balanced everywhere in the model domain.

146 The main aim of our study is to better understand the fundamental coupling of  
147 dehydration reactions, fluid flow and rock deformation, for which a simplified model is  
148 useful. Particular aims of our study are (1) to test the hypothesis for the shear-driven  
149 formation of olivine veins, (2) to quantify the mechanisms that control the porosity evolution  
150 and fluid pressure during dehydration of rocks and (3) to quantify the impact of shearing rate  
151 and kinetic reaction rate on the growth of dehydration veins.

152

## 153 **2. Mathematical model**

### 154 *2.1. Porous medium densities*

155 We consider a simple MSH system and the reaction antigorite (Mg<sub>48</sub>Si<sub>134</sub>O<sub>85</sub>(OH)<sub>62</sub>) +  
156 20 brucite (Mg(OH)<sub>2</sub>) = 34 forsterite (Mg<sub>2</sub>SiO<sub>4</sub>) + 51 water (H<sub>2</sub>O). We assume that antigorite  
157 and brucite together represent one solid rock phase with a homogeneous solid density,  $\rho_s$  (in  
158 kg/m<sup>3</sup>), and homogeneous material properties. All model parameters and variables are  
159 presented in Table 1. The total density of the porous rock, either consisting of antigorite +  
160 brucite or forsterite + water, is

161 
$$\rho_T = \rho_f \phi + \rho_s (1 - \phi) \quad (1)$$

162 with porosity  $\phi$  (volume ratio) and pore-fluid density  $\rho_f$ . For simplicity, we assume that the  
 163 solid phase consists of two components, (1) the non-volatile components, MgO and SiO<sub>2</sub>, that  
 164 remain always in the solid and (2) the volatile component, H<sub>2</sub>O, that is liberated during  
 165 dehydration. We quantify the amount of the non-volatile component as a function of MgO  
 166 inside the solid with its solid mass (in kg) fraction,  $X_s$ , which is  $X_s = 0.74$  (68 times the  
 167 molar mass of MgO / (68 times the molar mass of MgO + 51 times the molar mass of H<sub>2</sub>O) )  
 168 for the solid made of antigorite + brucite in a molar ratio of 1/20. Equivalently,  $X_s = 1$  for  
 169 forsterite. We neglect the SiO<sub>2</sub> in the calculations, because the SiO<sub>2</sub> for the considered  
 170 reaction cannot vary independently from MgO. The relative density of the solid MgO  
 171 component in the solid phase is

172 
$$\rho_X = \rho_s X_s \quad (2)$$

173 *2.2. Hydro-chemical model*

174 The conservation of mass (per unit volume) of the solid and the fluid is given by  
 175 respectively (e.g., McKenzie, 1984)

176 
$$\frac{\partial(\rho_s(1-\phi))}{\partial t} + \nabla[\rho_s(1-\phi)\mathbf{v}^s] = -\Gamma \quad (3)$$

177 
$$\frac{\partial(\rho_f\phi)}{\partial t} + \nabla[\rho_f\phi\mathbf{v}^f] = \Gamma \quad (4)$$

178 where  $t$  is time,  $\nabla$  is the divergence operator,  $\mathbf{v}^f$  and  $\mathbf{v}^s$  are vectors of the fluid and solid  
 179 barycentric velocities, respectively, and  $\Gamma$  is a dehydration rate that quantifies the rate at  
 180 which mass is transferred from the solid to the fluid phase. Concerning the symbols for vector  
 181 and tensor quantities, we use indices  $f$  and  $s$  as superscripts, because vector and tensor

182 components will have additional subscripts indicating the spatial direction, and scalar  
 183 quantities can be easier distinguished from vector and tensor quantities. Here, we do not use  
 184 two separate mass conservation equations for solid and fluid, but use the conservation  
 185 equation of total mass which results from the sum of equations (3) and (4) (e.g., Fowler, 1985;  
 186 Beinlich et al., 2020; Malvoisin et al., 2021; Plümper et al., 2016; Schmalholz et al., 2020):

$$187 \quad \frac{\partial \rho_T}{\partial t} + \nabla \left[ \rho_f \phi (\mathbf{v}^f - \mathbf{v}^s) \right] + \nabla (\rho_T \mathbf{v}^s) = 0 \quad (5)$$

188 The relative velocity of the fluid to the solid,  $\mathbf{v}^f - \mathbf{v}^s$ , in equation (5) is expressed by Darcy's  
 189 law in the absence of gravity

$$190 \quad \phi (\mathbf{v}^f - \mathbf{v}^s) = -\frac{k\phi^3}{\eta_f} \nabla p_f \quad (6)$$

191 where  $k$  is the permeability coefficient in a Kozeny–Carman-type permeability expression,  
 192  $\eta_f$  is the fluid viscosity and  $p_f$  is the fluid pressure. We need two mass conservation  
 193 equations because we consider two phases, solid and fluid. In addition to the conservation of  
 194 total mass, we use the conservation of the total non-volatile component (MgO) which is  
 195 described by

$$196 \quad \frac{\partial}{\partial t} [\rho_X (1 - \phi)] + \nabla [\rho_X (1 - \phi) \mathbf{v}^s] = 0. \quad (7)$$

197 There is no fluid velocity in this conservation equation because we assume that the dissolution  
 198 of MgO in the fluid is negligible.

199 We consider a constant temperature and a closed system with constant system  
 200 composition for the whole model domain, however, H<sub>2</sub>O can migrate within our model  
 201 domain. It has been experimentally demonstrated that dehydration reactions are controlled by

202 fluid pressure (e.g., Llana-Fúnez et al., 2012) and, therefore, we approximate  $\rho_s$ ,  $\rho_f$  and  $X_s$   
 203 as a function of  $p_f$ , which is expressed as (Schmalholz et al., 2020):

$$\begin{aligned}
 \rho_f &= \rho_f^{EQ}(p_f) \\
 \rho_s &= \rho_s^{EQ}(p_f) , \\
 X_s &= X_s^{EQ}(p_f)
 \end{aligned}
 \tag{8}$$

205 whereby the values of  $\rho_s^{EQ}$ ,  $\rho_f^{EQ}$  and  $X_s^{EQ}$  for a range of values of  $p_f$  are calculated by  
 206 equilibrium Gibbs free-energy minimization (e.g., Connolly, 2005, 2009; Fig. 3), using the  
 207 thermodynamic dataset of Holland and Powell (1998). We assume that  $\rho_f$  always  
 208 corresponds to  $\rho_f^{EQ}$ , as a result of its equation of state (Fig. 3C). Due to the sharp, step-like  
 209 variation of  $\rho_s^{EQ}$  and  $X_s^{EQ}$  with varying  $p_f$  across the dehydration reaction (Fig. 3C and D)  
 210 we assume that the reaction is controlled by a kinetic reaction timescale, so that values of  $\rho_s$   
 211 do not change instantaneously if  $p_f$  crosses the value of the reaction pressure at 12.65 kbar  
 212 (Fig. 3). The kinetic reaction timescales relevant to thermodynamic equilibrium are (e.g.,  
 213 Omlin et al., 2017)

$$\begin{aligned}
 \frac{\partial \rho_s}{\partial t} &= \frac{\rho_s^{EQ} - \rho_s}{t_{kin}} \\
 \frac{\partial X_s}{\partial t} &= \frac{X_s^{EQ} - X_s}{t_{kin}}
 \end{aligned}
 \tag{9}$$

215 where  $t_{kin}$  is the characteristic kinetic timescale. Employing an effective kinetic timescale for  
 216 the considered reaction allows us to quantify the impact of reaction kinetics on the model  
 217 results. Furthermore, the simulations are numerically more stable because the kinetic  
 218 formulation resolves better the temporal transition of the reaction and prohibits potentially

219 strong density oscillations for numerical grid points where values of  $p_f$  are very close to the  
 220 reaction pressure.

221

### 222 2.3. Mechanical model

223 The solid part of the 2D porous medium is behaving in a visco-plastic manner under  
 224 shear deformation. We assume that the shear viscosity is an exponential function of the  
 225 porosity (e.g., Schmeling et al., 2012). There are other possible porosity-viscosity relations,  
 226 but for simplicity we apply here only one of these relations. The relations between the  
 227 deviatoric stress tensor components,  $\tau_{ij} = \sigma_{ij} + p\delta_{ij}$  (where  $\sigma_{ij}$  are the components of the total  
 228 stress tensor,  $p$  is total pressure and  $\delta_{ij}$  is the Kronecker delta) and solid velocity gradients,  
 229 or deviatoric strain rate tensor components  $D_{ij}$ , are then

$$230 \quad \tau_{ij} = 2\eta_{s0} \exp[-30(\varphi - \varphi_0)] D_{ij} = 2\eta_s D_{ij} \quad (10)$$

231 where subscripts  $i$  and  $j$  are either 1 (representing the horizontal x-direction) or 2  
 232 (representing the vertical y-direction),  $\eta_{s0}$  is the reference solid shear viscosity for the initial  
 233 porosity,  $\varphi_0$ , and  $D_{ij} = (\partial v_i^s / \partial x_j + \partial v_j^s / \partial x_i) / 2 - \delta_{ij} (\partial v_i^s / \partial x_i) / 3$ . The  $\eta_s$  represents the  
 234 effective, porosity-dependent shear viscosity of the porous rock. The factor 30 was  
 235 determined by experiments with olivine-melt mixtures (e.g., Schmeling et al., 2012). We  
 236 further apply for one simulation a von Mises yield stress,  $\tau_y$ , to limit the maximal value of the  
 237 deviatoric stresses. The square root of the second invariant of the deviatoric stress tensor,  
 238  $\tau_{II} = \sqrt{0.5(\tau_{xx}^2 + \tau_{yy}^2) + \tau_{xy}^2}$  controls a plastic multiplier,  $\vartheta = 1 - \tau_y / \tau_{II}$ . If  $\vartheta > 0$ , then  
 239 deviatoric stresses are modified using

240 
$$\tau_{ij} = (1 - \vartheta) \tau_{ij}^s. \quad (11)$$

241 This von Mises plasticity prohibits that stresses locally increase to unrealistically high values.

242 Furthermore, we consider a poro-visco-elastic volumetric deformation for which the

243 divergence of the solid velocity field is a function of total pressure,  $p$ , and fluid pressure,  $p_f$

244 (e.g., Yarushina and Podladchikov, 2015):

245 
$$\nabla \mathbf{v}^s = -\frac{1}{K_d} \left( \frac{dp}{dt} - \alpha \frac{dp_f}{dt} \right) - \frac{p - p_f}{(1 - \phi) \lambda} \quad (12)$$

246 where  $\lambda$  is the bulk viscosity,  $K_d$  is the drained bulk modulus, and  $\alpha = 1 - K_d / K_s$  with  $K_s$

247 being the solid bulk modulus. The applied equations for conservation of total linear

248 momentum (or force balance equations) without inertial forces and gravity are

249 
$$\nabla \sigma_{ij} = 0 \quad (13)$$

#### 250 2.4. Governing system of equations

251 The above equations represent a system of 11 equations for 11 unknowns, which are  $p_f$ ,

252  $\phi$ ,  $\rho_s$ ,  $\rho_f$ ,  $X_s$ ,  $p$ ,  $v_x^s$ ,  $v_y^s$ ,  $\tau_{xx}$ ,  $\tau_{yy}$  and  $\tau_{xy}$ , assuming that the deviatoric stress tensor is

253 symmetric,  $\tau_{xy} = \tau_{yx}$ . The deviatoric stress tensor components,  $\tau_{xx}$ ,  $\tau_{yy}$  and  $\tau_{xy}$ , are calculated

254 using equations (10). The solid and fluid densities and the mass fraction are calculated from

255 the fluid pressure using equation (8) (see also equation (16) below and Fig. 3C and D).

256 Equation (5) is used to determine the fluid pressure,  $p_f$ , equation (12) to determine total

257 pressure,  $p$ , equation (7) to determine the porosity,  $\phi$ , and the two force balance equations

258 (13) to determine the two solid velocities,  $v_x^s$  and  $v_y^s$ . To determine  $p_f$ ,  $p$ ,  $\phi$ ,  $v_x^s$  and  $v_y^s$  we

259 employ the iterative pseudo-transient (PT) finite difference method described in detail in

260 Schmalholz et al. (2020). The PT equations are

261

$$\begin{aligned}
\frac{\Delta^{PT} p_f}{\Delta t_{pf}^{PT}} &= -\frac{\partial \rho_T}{\partial t} + \nabla \left[ \rho_f \frac{k\phi^3}{\eta_f} \nabla p_f \right] - \nabla (\rho_T \mathbf{v}^s) \\
\frac{\Delta^{PT} \phi}{\Delta t_\phi^{PT}} &= \frac{\partial}{\partial t} [\rho_X (1-\phi)] + \nabla [\rho_X (1-\phi) \mathbf{v}^s] \\
\frac{\Delta^{PT} v_i^s}{\Delta t_v^{PT}} &= \nabla \sigma_{ij} \\
\frac{\Delta^{PT} p}{\Delta t_p^{PT}} &= -\nabla \mathbf{v}^s - \frac{1}{K_d} \left( \frac{dp}{dt} - \alpha \frac{dp_f}{dt} \right) - \frac{p - p_f}{(1-\phi)\lambda}
\end{aligned} \tag{14}$$

262 When the discrete PT time derivatives of the left-hand sides of the equations (14) converge  
263 towards zero during iterations, then the corresponding steady-state equations on the right-  
264 hand sides are solved. The closed system of governing equations is given by equations (8),  
265 (10), (12) and (14).

266

## 267 2.5. Model configuration

268 We assume that  $p_f$  and  $p$  are initially identical. The porosity is 2%, except in an  
269 elliptical region in the model center where the porosity exhibits a Gaussian distribution with a  
270 maximal value of 16% (Fig. 4). The initial Gaussian distribution of the porosity is:

271  $\phi_0 = 0.02 + 0.14 \exp \left[ -(x/r)^2 - (y/2r)^2 \right]$ . The distance  $r$  controls the width, or variance, of

272 the porosity distribution which has an elliptical form with an axis ratio of 2 and with the long  
273 axis parallel to the vertical y-direction (Fig. 4). The origin of the coordinate system is at the  
274 center of the elliptical region with positive coordinates indicating towards the right side and  
275 upwards (Fig. 4). The shear and bulk viscosities are smaller in the central region due to the  
276 higher porosity. We assume a constant temperature of 500 °C for which the thermodynamic  
277 reaction pressure in our model is at 12.65 kbar (Fig. 3). The exact temperature value is not  
278 essential for our isothermal study, because the variation of the solid and fluid densities with

279 varying fluid pressure is similar for temperatures between 450 and 550 °C (Fig. 3A and B).  
280 The initial values of  $p_f$  and  $p$  are everywhere equal to 12.75 kbar, which is a pressure value  
281 slightly above the thermodynamic reaction pressure (Fig. 3A and B). We apply far-field  
282 simple shear for the boundary velocities (Fig. 4) so that the divergence, or volume change, of  
283 the entire model domain is zero. Shearing is parallel to the horizontal x-direction and, hence,  
284 orthogonal to the long axis of the elliptical region with elevated porosity (Fig. 4). Boundary  
285 conditions for  $\phi$  and  $p_f$  are of Dirichlet type, with boundary values fixed to the initial  
286 ambient values.

287

## 288 *2.6. Numerical algorithm and dimensionless parameters*

289 All partial derivatives are approximated with discrete difference ratios following the  
290 standard procedure of staggered finite difference (FD) methods (e.g., Gerya, 2019). The  
291 numerical algorithm consists of an outer time loop containing an internal PT iteration loop  
292 (Schmalholz et al., 2020). The PT iteration procedure aims at minimizing the PT time  
293 derivatives, i.e. the left-hand sides in the discretized equations (14). The iteration procedure is  
294 stopped when the PT time derivatives reach a predefined tolerance, here  $10^{-8}$ . The iterative  
295 implicit PT solution of the discretised system of equations (14) requires the definition of four  
296 numerical pseudo time steps,  $\Delta t^{PT}$ , namely,  $\Delta t_{pf}^{PT}$ ,  $\Delta t_p^{PT}$ ,  $\Delta t_\phi^{PT}$ , and  $\Delta t_v^{PT}$  to solve for  $p_f$ ,  $p$ ,  
297  $\phi$ , and  $v_x^s$  and  $v_y^s$ , respectively. The physical time step,  $\Delta t$ , controls the evolution of the  
298 system in physical time for which we implicitly solve. The applied numerical time steps are  
299 specified in appendix A1.

300 There are many possibilities to scale and non-dimensionalize the model parameters inside  
301 the numerical algorithm. We programmed the numerical algorithm in such a way that the

302 specific magnitudes of individual parameters, such as shear viscosity, are not significant and  
 303 that the characteristic physical behaviour of the system is controlled by dimensionless  
 304 parameters. This scaling provided also the most stable convergence during the PT iterations.  
 305 The applied dimensionless parameters and numerical examples applied in the simulations are:

$$\begin{aligned}
 \Omega_1 &= \frac{w}{r} & e.g. \quad \Omega_1 &= \frac{4m}{10^{-1}m} = 40 \\
 \Omega_2 &= \frac{k \eta^s}{\eta_f r^2} & e.g. \quad \Omega_2 &= \frac{10^{-22} m^2}{10^{-3} Pas} \frac{10^{18} Pas}{(10^{-1}m)^2} = 10 \\
 \Omega_3 &= \frac{\lambda}{\eta^s} & e.g. \quad \Omega_3 &= \frac{2 \times 10^{18} Pas}{10^{18} Pas} = 2 \\
 \Omega_4 &= \frac{\bar{D}_{xy} \eta^s}{p_{ini}} & e.g. \quad \Omega_4 &= \frac{1.12 \times 10^{-10} s^{-1} 10^{18} Pas}{12.75 \times 10^8 Pa} = 0.0878
 \end{aligned} \tag{15}$$

307 where  $w$  is the model width and  $\bar{D}_{xy}$  is the applied far-field simple shear rate (Fig. 4). The  
 308 values of the applied parameters are discussed in section 4.

309 For reasons of numerical efficiency, we approximate the thermodynamic relations of the  
 310 densities and mass fractions with the fluid pressure, obtained with Gibbs free-energy  
 311 minimization, with analytical functions (Fig. 3C and D):

$$\begin{aligned}
 \rho_f &= 1194 \times \ln \left( \frac{p_f}{p_{ini}} + 1 \right)^{1/3.5} \\
 \rho_s &= -\tanh \left( 600 \times \frac{p_f - p_R}{p_{ini}} \right) \times 323.32 + 2848 + \left( \frac{p_f}{p_{ini}} - 0.0078 \right) \times 30.4762 \\
 X_s &= -\tanh \left( 600 \times \frac{p_f - p_R}{p_{ini}} \right) \times 0.1292 + 0.8707
 \end{aligned} \tag{16}$$

313 where  $p_R$  is the reaction pressure, here 12.65 kbar. We use the functions above in the  
 314 numerical algorithm to calculate densities and mass fraction from the current fluid pressure.

315

### 316 3. Results

#### 317 3.1. Scaling and presentation of results

318 We present most quantities in dimensionless form to emphasize their general validity. For  
319 example, all distances are made dimensionless by dividing them by  $r$  and all times are made  
320 dimensionless by dividing them with the characteristic time  $t_c = r^2 \eta_f / (k K_s)$ . Consequently,  
321 all velocities are made dimensionless by dividing them by the characteristic velocity  $r / t_c$ . In  
322 contrast, since we consider a particular metamorphic reaction, we display the densities and  
323 pressures in dimensional units.

#### 324 3.2. Dehydration vein formation under simple shear

325 For the first simulation presented here, we use the dimensionless parameters and  
326 specific parameter values given in equation (15). The numerical resolution is 900×900 grid  
327 points in the x- and y-direction, respectively. A numerical resolution test is given in appendix  
328 A2. The coupling of the dehydration reaction, fluid flow and solid deformation is controlled  
329 by four characteristic time scales: a time scale related to fluid pressure diffusion,  
330  $t_{dif} = r^2 \eta_f / (k \phi_0^3 K_s)$ , a time scale related to the applied far-field deformation,  $t_{def} = 1 / \bar{D}_{xy}$ , a  
331 time scale related to the mineral-reaction kinetics,  $t_{kin}$  (equation (9)), and a time scale related  
332 to viscoelastic stress relaxation,  $t_{rel} = \eta_s / K_s$ . We assume here  $K_s = 10^{11}$  Pa which, for the  
333 parameter values in equation (15), yields  $t_{rel} / t_{def} \sim 10^{-3}$  and indicates that the deformation is  
334 effectively viscous since  $t_{rel}$  is significantly shorter than  $t_{def}$ . The ratio  $t_{rel} / t_{def}$  is commonly  
335 referred to as Deborah number (e.g. Reiner, 1964; Moulas et al., 2019). For the first  
336 simulation,  $t_{def} / t_{dif} = 0.071$  and  $t_{kin} / t_{dif} = 0.0025$  so that both the characteristic times for  
337 shearing and reaction kinetics are shorter than the characteristic time of diffusive fluid flow.

338 The ratio  $t_{kin} / t_{dif}$  is similar to a Damköhler number since it relates the characteristic time of  
339 mineral reactions to the characteristic time of transport by diffusive fluid flow. The central  
340 region with initially higher porosity (Fig. 5E) represents a mechanically weak inclusion  
341 because the shear and bulk viscosity decrease with increasing porosity. The applied far-field  
342 simple shear causes variations in  $p_f$  around the weak region and the numerical results for the  
343 first time step show two regions in which  $p_f$  is smaller than the reaction pressure of 12.65  
344 kbar (black contours in Fig. 5A). Therefore, dehydration is triggered in these two regions of  
345 decreased  $p_f$ . The dehydration causes the release of water, consequently an increase in  
346 porosity and, hence, a decrease of viscosity. With progressive simple shearing these  
347 dehydrating regions grow in the direction parallel to the maximal principal stress,  $\sigma_1$ , which  
348 is oriented 45 degrees with respect to the shearing direction (Fig. 5E). The maximal and  
349 minimal,  $\sigma_3$ , principal stresses have been calculated using the algorithm of Spitz et al. (2020),  
350 which was originally developed to calculate principal strain directions. During progressive  
351 shearing, two dehydrating regions evolve and form vein-like regions with increased values of  
352  $\rho_s$  and  $\phi$  (Fig. 5). The total solid velocity field (grey arrows in Fig. 5A to D) indicates the  
353 applied far-field simple shear and local deviations from the horizontal shear direction. For the  
354 specific parameters given in equation (15) the maximal shear stresses are ca. 125 MPa. We  
355 also calculate the distance between the highest (in vertical y-direction) and the lowest point on  
356 the contours for  $p_f = 12.65$  kbar (red straight lines in Fig 5A to D). We will use this distance  
357 as a proxy for the change in length of the dehydrating region representing the length of the  
358 dehydration vein. During progressive shearing, the value of  $\rho_s$  in the dehydration region  
359 increases from initially ca. 2550 kg m<sup>-3</sup> to ca. 3100 kg m<sup>-3</sup> which represents the transformation  
360 from antigorite + brucite to forsterite (Figs. 3C and 5A to D). In the region of the two  
361 forsterite veins, the associated values of  $\phi$  increase from initially 2% to ca. 60% (Fig. 5E to

362 H). Two representative contours of  $\phi$ , for 5 and 15%, highlight two features of the evolution  
363 of  $\phi$ : the growth of high-porosity dehydration veins and the clock-wise rotation of the initial  
364 porosity field due to the applied simple shear (Fig. 5E to H).

365

### 366 *3.3. Dehydration vein formation for faster deformation rate and plastic yield stress*

367 We perform a second simulation with the same parameters as the first simulation, except that  
368 we apply now a different value of  $t_{def}$  which provides  $t_{def} / t_{dif} = 0.038$  (Fig. 6A to D)  
369 generating a faster shearing since the characteristic time of deformation is shorter. The main  
370 difference to the simulation with  $t_{def} / t_{dif} = 0.071$  (Fig. 5) is that the two dehydration regions  
371 connect during progressive shearing to form a single dehydration vein (Fig. 6D). For the  
372 specific parameters given in equation (15) the maximal shear stresses are ca. 220 MPa. We  
373 perform a third simulation with the same parameters as in the second simulation and apply a  
374 von Mises yield stress of 150 MPa (Fig. 6E to H). With such yield stress, a single dehydration  
375 vein also forms but the vein is shorter and thicker for the same simulated times (Fig. 6). The  
376 performed three simulations result in a similar development of dehydration veins with  
377 forsterite, but show that different deformation rates and the application of a yield stress impact  
378 the geometry and length of the veins.

379

### 380 *3.4. Coupling of dehydration reaction, fluid flow and solid deformation*

381 To better understand and visualize the coupling between the dehydration reaction, fluid flow  
382 and solid deformation we show the distribution and evolution of various quantities on a single  
383 figure (Fig. 7). We use the results of the first simulation (Fig. 5) and we focus on one  
384 dehydration region in the area to the top-left of the model center (Fig. 7). The divergence of

385 the solid velocity,  $\nabla \mathbf{v}^s = \partial v_x^s / \partial x + \partial v_y^s / \partial y$ , indicates a volumetric change associated with  
386 dehydration vein formation (Fig. 7). A positive value of  $\nabla \mathbf{v}^s$  indicates volume increase, or  
387 dilation (blue colors in Fig. 7). Overall, the solid velocities indicate the applied far-field  
388 simple shear deformation (blue arrows in Fig. 7), with some deviations around the  
389 dehydrating region. The fluid velocities (red arrows in Fig. 7) are completely different  
390 compared to the solid velocities. For the first time step, fluid flow only occurs in the central  
391 region where the porosity, and hence permeability, is high (Fig. 7A). During dehydration vein  
392 formation, fluid flow mainly occurs in the region of the veins where significant dilation takes  
393 places (Fig. 7B to D). The fluid velocities indicate fluid flow from the boundary of the  
394 dehydrating region towards the centre of the vein (Fig. 7C). In other words, fluid is released  
395 during dehydration from the surrounding serpentinite and the released fluid flows into the  
396 vein. For the first time step, the porosity distribution indicates the initial, Gaussian-type,  
397 porosity distribution (blue contours in Fig. 7). With progressive deformation and vein  
398 formation, the high-porosity region grows in the direction of the dehydration vein, indicated  
399 by significant dilation and fluid flow. At the beginning of shearing, a larger region with fluid  
400 pressure (red contours in Fig. 7)  $< 12.65$  kbar corresponds more or less to the region of  
401 significant dilation (Fig. 7A). The solid densities (dashed grey contours in Fig. 7) increase  
402 during the progressive dehydration reaction and the transformation from antigorite + brucite  
403 to forsterite (Fig. 7B to D). The values of solid density increase with time due to the applied  
404 mineral-reaction kinetics which avoids that the density changes instantaneously once the fluid  
405 pressure decreases locally below 12.65 kbar. With progressive vein formation, fluid pressures  
406 below 12.65 kbar only exist in the region of significant dilation, fluid flow and increased  
407 values of solid density (Fig. 7).

408

409 3.5. Mechanisms controlling porosity variation and fluid pressure

410 In our coupled HMC model, the temporal variation of porosity is controlled by several  
 411 mechanisms, such as volumetric deformation of the solid or mass transfer due to the  
 412 dehydration reaction. To quantify the relative contribution of the mechanisms controlling the  
 413 temporal variation of porosity, we post-process our numerical results (i.e. calculate values  
 414 from saved numerical results). We quantify the mass transfer rate,  $\Gamma$ , associated with the  
 415 dehydration reaction, which can be expressed by (using equation (3)):

$$416 \quad \Gamma = -\frac{d(\rho_s(1-\phi))}{dt} - \rho_s(1-\phi)\nabla\mathbf{v}^s. \quad (17)$$

417 Note that in equation (17) the material time derivative ( $d/dt$ , including the advection term,  
 418  $\mathbf{v}^s\nabla[\rho_s(1-\phi)]$ ) is used and, hence, the divergence term is different compared to equation (3)  
 419 . Therefore, equation (17) represents an approximation of  $\Gamma$  since the advective term is not  
 420 taken into account, here for simplicity of the post-processing. Equation (17) can be rearranged  
 421 to provide an expression for the temporal variation of the porosity:

$$422 \quad \frac{1}{(1-\phi)}\frac{d\phi}{dt} = \nabla\mathbf{v}^s + \frac{1}{\rho_s}\frac{d\rho_s}{dt} + \frac{\Gamma}{\rho_s(1-\phi)} \quad (18)$$

423 Equation (18) shows that the temporal variation of the porosity is controlled by three  
 424 mechanisms: (1) volumetric deformation of the solid (i.e. divergence of velocity field; first  
 425 term on right-hand side of equation (18)), (2) temporal variation of solid density (second  
 426 term) and (3) mass transfer of H<sub>2</sub>O from the solid to the fluid phase associated with the  
 427 dehydration reaction (third term). We display the spatial distribution of the four terms in  
 428 equation (18) for the first simulation at a dimensionless time of 0.7 (Fig. 8). The temporal  
 429 variation of porosity, quantified by the term on the left-hand side of equation (18), is positive  
 430 and largest in the region of increased porosity, indicating an increase in porosity with time

431 (Fig. 8A). Each of the three terms on the right-hand side of equation (18) can be calculated  
 432 from the saved numerical results (Fig. 8C to E) and their sum (Fig. 8B) provides essentially  
 433 the same result as the term on the left-hand side of equation (18) (Fig. 8A). The results show  
 434 that the magnitudes of the relative contributions of volume change (Fig. 8C), solid density  
 435 variation (Fig. 8D) and mass transfer (Fig. 8E) to the temporal variation of porosity are  
 436 similar. Therefore, volume change, solid density variation and mass transfer equally  
 437 contribute to the porosity variation and, hence, for the evolution of the dehydration veins.

438 We also investigate the porosity variation for a simulation which has the same value of  
 439  $t_{def} / t_{dif} = 0.071$  as the first simulation, but with a slower kinetic-reaction rate (or longer  
 440 reaction time) of  $t_{kin} / t_{dif} = 0.022$  for a dimensionless time of 1.0 (Fig. 9). The magnitude of  
 441 the temporal porosity variation is now slower (compare Fig. 8A and 9A) but the relative  
 442 contribution of volume change, solid density variation and mass transfer to the porosity  
 443 variation is again similar. Therefore, different kinetic reaction rates change the magnitude of  
 444 the temporal porosity variation, but do not change the relative importance of volume change,  
 445 density variation and mass transfer controlling the porosity evolution.

446 Similar to the temporal variation of  $\phi$ , the distribution of  $p_f$  is also controlled by  
 447 several mechanisms and variables. To quantify the mechanisms controlling  $p_f$ , we post-  
 448 process again our numerical results. Substituting equation (12), which defines  $\nabla \mathbf{v}^s$ , into  
 449 equation (18) and solving for  $p_f$  yields

$$450 \quad p_f = p + \frac{\lambda(1-\phi)}{K_d} \left( \frac{dp}{dt} - \alpha \frac{dp_f}{dt} \right) + \lambda \frac{d\phi}{dt} - \frac{\lambda(1-\phi)}{\rho_s} \frac{d\rho_s}{dt} - \frac{\lambda}{\rho_s} \Gamma. \quad (19)$$

451 Equation (19) shows that  $p_f$  is controlled by five mechanisms and quantities: (1) the  
 452 magnitude of  $p$  (first term on the right-hand side of equation (19)), (2) elastic deformation

453 involving the temporal variation of  $p$  and  $p_f$  (second term), (3) temporal variations in  
454 porosity (third term), (4) temporal variations of solid density (fourth term) and (5) mass  
455 transfer by dehydration (fifth term). We display the spatial distribution of all terms in equation  
456 (19) for the first simulation at a dimensionless time of 0.7 (Fig. 10). The distribution of  $p_f$  is  
457 mainly controlled by the distribution of  $p$  (Fig. 10A and C). The distribution of  $p_f$  can be  
458 accurately post-processed by summing up the five terms on the right-hand side of equation  
459 (19) (Fig. 10B). The mass transfer (Fig. 10E), the porosity variation (Fig. 10F) and the solid  
460 density variation (Fig. 10G) have an approximately equal impact on the distribution of  $p_f$ ,  
461 but their contributions are significantly smaller compared to the contribution of  $p$ . The  
462 contribution of elastic volumetric deformation (Fig. 10H) is essentially negligible, since it is  
463 three orders of magnitude smaller than the magnitude of  $p_f$ . For the presented simulation, the  
464 maximal value of the deviatoric stress invariant,  $\tau_{II}$  (equation (11)), in the model domain is  
465 ca. 140 MPa (Fig. 10D).

466

### 467 *3.6. Impact of kinetic reaction rate and shearing rate on vein evolution*

468 We performed in total ten simulations to investigate the impact of the far-field  
469 shearing rate and of the kinetic reaction rate on the evolution of dehydration veins and  
470 forsterite generation (Fig. 11). Six simulations had the same value of  $t_{kin} / t_{dif} = 0.0025$  but  
471 different values of  $t_{def} / t_{dif}$  (legend in Fig. 11A). The increase in length of the red line shown  
472 in figure 5A to D is used as a proxy for the temporal evolution of the vein length (Fig. 5A).  
473 The initial value of vein length is determined by the initial distribution of  $p_f$  (Fig. 5A). In  
474 regions with  $p_f < 12.65$  kbar the dehydration reaction is triggered, which causes a local

475 increase of H<sub>2</sub>O and an increase of  $p_f$  (Fig. 11B). For the six simulations, this initial increase  
476 of  $p_f$  generated values of  $p_f > 12.65$  kbar everywhere in the model domain, so that the vein  
477 length is zero (Fig. 11A and B). With progressive deformation, values of  $p_f$  decrease again  
478 below 12.65 kbar initiating the growth of a dehydration vein. The time until values of  $p_f$   
479 decrease below 12.65 kbar is longest for the simulation with the slowest far-field deformation  
480 rate (Fig. 11A). Consequently, the increase of  $\rho_s$  starts latest for the simulation with slowest  
481 far-field deformation rate (Fig. 11C). However, during significant increase of  $\rho_s$  the rate of  
482 increase (indicated by the slope of the density versus time lines) of  $\rho_s$  is similar for all  
483 simulations, because they considered the same mineral-kinetic rate ( $t_{kin} / t_{dif} = 0.0025$ ). The  
484 simulation with the fastest deformation rate (Fig. 6A to D; blue line in Fig. 11A to C) was run  
485 a second time, but then with a von Mises yield stress (Fig. 6E to F; dashed blue line in Fig.  
486 11A to C). The application of the yield stress slows down the vein growth, but has no  
487 significant impact on the evolution of  $\rho_s$  (Fig. 11C). The temporal evolution of the vein  
488 length shows that the veins grow fast at the onset of vein formation and then vein growth  
489 slows down progressively (Fig. 11A) because the minimum values of  $p_f$  in the model  
490 increase progressively (Fig. 11B) due to ongoing fluid flow which reduces gradients of  $p_f$ .

491 We performed four simulations for the same value of  $t_{def} / t_{dif} = 0.071$  but for four different  
492 values of  $t_{kin} / t_{dif}$  (legend in Fig. 11D). The vein growth is similar for the four simulations  
493 (Fig. 11D), however, the increase of  $\rho_s$  is significantly different due to the different mineral-  
494 reaction rates (Fig. 11F). The values of  $\rho_s$  increase fastest for the fastest reaction rate (Fig.  
495 11F), but values of  $p_f$  vary less during deformation for faster reaction rates (Fig. 11E). For  
496 slow reaction kinetics,  $t_{kin} / t_{dif} = 0.022$  (Fig. 11F), maximal values of  $\rho_s$  did not reach 2800

497 kg m<sup>-3</sup> hindering the complete formation of forsterite when the vein growth has essentially  
498 stopped (corresponding blue line in Fig. 11D). The results for different kinetic rates suggest  
499 that the kinetic reaction rate must be significantly faster than the pressure diffusion rate to  
500 allow the complete transformation from antigorite + brucite to forsterite during dehydration  
501 and vein growth, while fluid pressures are in the forsterite stability field.

502

#### 503 **4. Discussion**

504 The performed simulations show that it is hydrologically, mechanically and  
505 chemically feasible to form olivine veins by dehydration reactions during ductile shearing of  
506 serpentinite. In the scenario studied here, dehydration is shear-driven and triggered by fluid  
507 pressure perturbations caused by heterogeneities in porosity-dependent effective viscosity.  
508 The resulting veins grow in a direction parallel to the maximal principal stress and no  
509 fracturing is required for vein formation and growth. The simulations show that the two  
510 dimensionless ratios  $t_{def} / t_{dif}$  and  $t_{kin} / t_{dif}$  control the temporal evolution of the dehydration  
511 vein length, the fluid pressure and the solid density (Fig. 11). In our simulations both the  
512 values of  $t_{def}$  and  $t_{kin}$  need to be significantly shorter than  $t_{dif}$  (Fig. 11). To test the  
513 applicability of our simulations to sheared serpentinite at subduction zones, we estimate the  
514 value of  $t_{dif} = r^2 \eta_f / (k \phi_0^3 K_s)$  using the parameter values specified in equation (15) and the  
515 initial porosity of 2%. The least constrained parameter in  $t_{dif}$  is likely the effective  
516 permeability,  $k \phi_0^3$ , which in our simulations would be  $10^{-22} m^2 \times 0.02^3 = 8 \times 10^{-28} m^2$ .  
517 Experimental studies suggest that serpentinite permeability decreases exponentially with  
518 depth and is in the order of  $10^{-23}$  and  $10^{-21} m^2$  at a depth of 7 km below seafloor (e.g.  
519 Hatakeyama et al., 2017). Using the extrapolation of Hatakeyama et al. (2017) (their equation

520 1) for their serpentinite termed Sengen-03 provides a permeability of  $10^{-30} \text{ m}^2$  for a confining  
 521 pressure of 9 kbar and  $10^{-35} \text{ m}^2$  for a confining pressure of 12.75 kbar, as applied here.  
 522 Therefore, an effective permeability in the order of  $10^{-27} \text{ m}^2$ , as used here, seems not  
 523 unrealistic for serpentinite under a confining pressure of 12.75 kbar and the assumed  
 524 temperature of 500 °C. For simplicity, we assume here an isotropic permeability, but in  
 525 natural serpentinite the permeability might be anisotropic. For the considered parameter  
 526 values we obtain  $t_{dif} = 1.25 \times 10^{11} \text{ s} \approx 4 \text{ kyr}$ . A representative value of  $t_{def}$  in our simulations is  
 527  $0.05 \times t_{dif}$  (Fig. 11A). The inverse of  $t_{def}$  corresponds to the applied far-field shearing rate,  
 528  $\bar{D}_{xy}$ , which is then  $1.6 \times 10^{-10} \text{ s}^{-1}$ . A shear strain rate in the order of  $10^{-10} \text{ s}^{-1}$  is feasible for  
 529 serpentinite shearing at a subduction plate interface (e.g. Chernak and Hirth, 2010). A  
 530 representative value of  $t_{kin}$  in our simulations forming forsterite is  $0.001 \times t_{dif}$  (Fig. 11D)  
 531 which corresponds to 4 years. Here, we assume a viscosity of serpentinite of  $10^{18} \text{ Pas}$ . Despite  
 532 the importance of serpentinite, its rheology at lithospheric-scale pressure and temperature  
 533 conditions remains not well constrained (David et al., 2018; Hirauchi et al., 2020, and  
 534 references therein). However, for the ambient pressure and temperature conditions considered  
 535 here, viscosities of serpentinite between  $10^{17}$  and  $10^{18} \text{ Pas}$  seem feasible based on  
 536 experimental studies (e.g., Chernak and Hirth, 2010; Hilairet et al., 2007). For the applied  
 537 parameter values, the characteristic time,  $t_c = r^2 \eta_f / (k K_s)$ , is ca. 12 days. The dimensionless  
 538 simulation times for the ten simulations are between 600 and 1500 (Fig. 11) which then  
 539 corresponds to a real time between approximately 20 and 50 years, respectively.

540 We consider here, for simplicity, a fixed chemical composition for which forsterite +  
 541 water results from dehydration of antigorite + brucite + a negligible amount of free water. We  
 542 consider this negligible amount of free water simply to be able to calculate thermodynamically  
 543 the fluid density in the stability field of antigorite + brucite (Fig. 3C). Natural chemical

544 compositions, in for example the Erro-Tobbio unit, are more complex and feature a higher  
545 chemical variability as considered in our model. However, the main aim of our study is to  
546 investigate the fundamental coupling between dehydration reactions, fluid flow and rock  
547 deformation, justifying the use of a simplified MSH system. Our model suggests that natural  
548 areas of serpentinite dehydration, consisting of olivine and water, are mechanically weak due  
549 to their high, up to 60%, porosity and water content. After the formation of the dehydration  
550 veins, the water eventually escapes the dehydration region, so that finally only olivine is left  
551 in the veins.

552         Field data show that in the Erro Tobbio region the olivine in the veins is metamorphic  
553 olivine which resulted from the dehydration of serpentinite. A dehydration origin of the  
554 olivine is supported by geochemical studies (e.g., Kempf et al., 2020; Peters et al., 2020).  
555 Furthermore, the particular en-échelon orientation of the olivine veins suggest that the vein  
556 orientation is controlled by the stress field associated with the serpentinite shearing (Hermann  
557 et al. 2000). Therefore, based on published geochemical studies and structural observations  
558 we propose that the formation of observed olivine veins was the result of a coupled  
559 deformation-reaction process that accelerated the mineral dehydration along particular  
560 orientations, controlled by the local stress field in the sheared serpentinite. Similar veins made  
561 of metamorphic olivine have been described from subducted serpentinite, such as in the  
562 Zermatt-Saas unit in the Central Alps (e.g., Kempf et al., 2020).

563         The initial distribution of porosity in the presented simulations is simple and defined  
564 by a Gaussian distribution. Such a simple initial porosity distribution is again useful to study  
565 the fundamental coupling of dehydration reactions and rock deformation. More realistic  
566 would likely be an initial random distribution of porosity. To test whether the studied  
567 formation of dehydration veins also occurs for a more realistic initial porosity distribution, we  
568 performed one simulation with an initial random porosity distribution. The initial values of

569 porosity vary randomly between 2 and 16% in the model domain. We generated the initial  
570 porosity distribution with the random field generator presented in Räss et al. (2019). For this  
571 simulation, we applied  $t_{def} / t_{dif} = 0.012$  and  $t_{kin} / t_{dif} = 8.2 \times 10^{-4}$ . Furthermore, the initial  
572 values for  $p$  and  $p_f$  are 12.73 kbar. All other parameters are identical to the values of the  
573 first simulation (Fig. 5). The simulation shows that during shearing many dehydration veins  
574 with increasing solid density and porosity are formed, similar to the simulations with an initial  
575 Gaussian porosity distribution (Fig. 12). Particularly, despite the variability in shape of the  
576 dehydrating regions, the longest axis of the dehydrating regions always grows in the direction  
577 of the maximum principal stress. Hence, the results with an initial random porosity  
578 distribution suggest that the investigated simulations with an initial Gaussian porosity  
579 distribution capture the first-order mechanisms of shear-driven dehydration vein formation for  
580 more complex and natural model configurations. Furthermore, the simulation shows the  
581 formation of many veins with similar length which is similar to observations from natural  
582 olivine veins (Fig. 1A to C). The generation of many similar veins results from the self-  
583 limiting nature of vein growth (Fig. 11A and D) which prohibits the generation of few large  
584 veins.

585         The presented model could potentially be applied to investigate fluid-related processes  
586 causing episodic tremor and slow-slip events (ETS; e.g., Peng & Gomberg 2010). Despite the  
587 lack of consensus on the inter-relationships between mineral dehydration, fluid flow, critical  
588 stress and ETS, the coincidence of the location of low-frequency earthquakes to regions with  
589 high  $V_p/V_s$  ratios requires the consideration of fluid flow and mineral dehydration in these  
590 settings (e.g., Burlini et al. 2009; Kato et al. 2010; Shelly et al. 2006; Van Avendonk et al.,  
591 2010). For example, Van Avendonk et al. (2010) infer a zone of very high  $V_p/V_s$  ratio of 6 at  
592 the top of the subducting Cocos slab between 35 and 55 km depth, lying downdip of the  
593 seismogenic zone. They propose that these high  $V_p/V_s$  ratios are due to several-meter thick

594 shear zones under high pore pressure and that the hydrous pore fluids were generated by  
595 prograde dehydration reactions. The 35 to 55 km depth range with inferred high  $V_p/V_s$  ratios  
596 corresponds to the depth range and ambient pressure considered in our model. In addition, the  
597 correlation of rapid-tremor migration to pore-pressure waves suggests that this coincidence  
598 can be explained by the coupled processes of dehydration, fault weakening and tremor  
599 migration (Cruz-Atienza et al. 2018). Thus, the formation of fluid-filled veins, as modelled  
600 here, can be correlated to the transient weakening that is inferred in regions of mineral  
601 dehydration. Furthermore, the dehydration reaction, generating olivine-fluid bearing veins,  
602 and the subsequent fluid escape, leaving behind olivine-only veins, will cause a viscosity  
603 inversion: when significant fluid is present in the olivine bearing veins, then the effective  
604 viscosity of the olivine-fluid veins is smaller than the viscosity of the serpentinite; but once  
605 the fluid has escaped the veins the effective viscosity of the olivine-only veins is larger than  
606 the viscosity of the serpentinite. We expect that, under the presence of a general anisotropic  
607 stress field, the vein formation will lead to an increase of the anisotropic effective viscosity of  
608 the subducted mantle rocks as a result of the different effective viscosities of serpentinite and  
609 olivine + fluid assemblages. When the fluid is completely drained from these veins, the  
610 viscosity contrast between olivine and serpentinite is such that the associated anisotropy will  
611 be permanent.

612

## 613 **5. Conclusions**

614 We present a hydro-mechanical-chemical model to investigate the reaction antigorite +  
615 brucite = forsterite + water. The model can explain shear-driven formation of dehydration  
616 veins in ductile serpentinite and, hence, supports the hypothesis of shear-driven formation of  
617 metamorphic olivine veins in the serpentinites of the Erro Tobbio unit (Fig. 1). Vein  
618 formation is triggered by fluid pressure perturbations caused by local perturbations of a

619 porosity-dependent effective viscosity. The veins consist of a weak forsterite-water mixture  
620 and grow in a direction parallel to the maximal principal stress which is controlled by the  
621 applied far-field simple shearing. The modelled growth of the dehydration veins is not a stable  
622 or runaway process but a self-limiting process because the fluid pressure perturbations that  
623 drive the vein growth decrease during progressive shearing due to fluid flow.

624 In our model, three characteristic time scales control the formation of dehydration  
625 veins: (1) The time scale of fluid pressure diffusion,  $t_{dif}$ , which controls porous fluid flow via  
626 Darcy's law, (2) the time scale of the far-field shearing,  $t_{def}$ , which is the inverse of the far-  
627 field shearing rate and (3) the time scale of the mineral-reaction kinetics,  $t_{kin}$ , which controls  
628 the time to achieve thermodynamic equilibrium. To form an olivine (here forsterite) vein, the  
629 kinetic reaction rate for the transformation from serpentinite to olivine must be fast enough so  
630 that olivine can form during vein growth, while significant fluid pressure perturbations exist.  
631 The numerical simulations suggest that the kinetic reaction rate should be at least two orders  
632 of magnitude faster than the characteristic rate of fluid pressure diffusion.

633 In our models, the temporal evolution of porosity during dehydration is controlled by  
634 three mechanisms: solid volume change, solid density variation and reactive mass transfer.  
635 All three mechanisms have a similar impact on the porosity evolution. Hence, our model  
636 shows that deformation of the solid rock should be considered when quantifying dehydration  
637 vein formation. The fluid pressure distribution is mainly controlled by the total pressure  
638 distribution. Mass transfer, porosity variation and solid density variation impact the fluid  
639 pressure distribution to a minor extent and only in the dehydrating region.

640 The presented model can help to understand the formation of olivine veins in  
641 serpentinite mylonites in subduction zones. Such veins are observed in several high pressure  
642 serpentinites in the Western Alps and Liguria. The modelled veins have a similar orientation  
643 as natural en-échelon olivine veins in serpentinite mylonite. The self-limiting feature of the

644 modelled vein growth might also explain the natural observation of many smaller olivine  
645 veins and the absence of few large olivine veins. Furthermore, the presented model can  
646 explain transient weakening during dehydration in deforming rock which may be an important  
647 process during episodic tremor and slow-slip observed in subduction zones.

648

## 649 **Acknowledgements**

650 S.M.S. is grateful for theoretical advices from Y. Podladchikov and for practical  
651 programming help of T. Duretz. This work was supported by the University of Lausanne.  
652 E.M. acknowledges the Johannes Gutenberg University of Mainz for financial support. L.R.  
653 acknowledges financial support from the Swiss University Conference and the Swiss Council  
654 of Federal Institutes of Technology through the Platform for Advanced Scientific Computing  
655 (PASC) program, obtained via the PASC project GPU4GEO. There is no conflict of interest.

656

## 657 **Availability Statement**

658 The software developed and used in the scope of this study is licensed under MIT  
659 License. The latest versions of the code is available for download from GitHub at:  
660 <https://github.com/PTsolvers/PseudoTransientHMC.jl> (last access: 18 May 2022). Past and  
661 future versions of the software are available from a permanent DOI repository (Zenodo) at:  
662 <https://doi.org/10.5281/zenodo.6559431> (Schmalholz and Räss, 2022). The codes are written  
663 using the Julia programming language and execute on graphical processing units (GPUs).  
664 Refer to the repository's README for additional information.

665

## 666 **Appendix**

### 667 **A1. Pseudo-transient time steps**

668 To solve the system of equations (14) iteratively, we apply the following physical,  $\Delta t$ ,  
 669 pseudo-transient (PT),  $\Delta t^{PT}$ , time steps:

$$\begin{aligned}
 \Delta t &= \frac{1}{2} \frac{r^2 \eta_f}{k K_s} \\
 \Delta t_{\phi}^{PT} &= \Delta t \\
 \Delta t_{pf}^{PT} &= \frac{1}{16.1} \frac{\max(\Delta x, \Delta y)^2}{\max\left(4 \frac{k \phi^3 K_s}{\eta_f}\right)} \\
 \Delta t_v^{PT} &= \frac{1}{24.15} \frac{\max(\Delta x, \Delta y)^2}{\max(\eta^s)} \\
 \Delta t_p^{PT} &= 471 \frac{\max(\eta^s) dx}{w}
 \end{aligned} \tag{A1}$$

671 where  $\Delta x$  and  $\Delta y$  are horizontal and vertical numerical grid spacing, respectively. More  
 672 information concerning the choice of such PT time steps can be found in Wang et al. (2022).

673

## 674 **A2. Numerical resolution test**

675 We present here the results of a numerical resolution test. Such test is essential to  
 676 determine whether the evolution of the dehydrating region is independent of the employed  
 677 numerical resolution. We performed the first simulation (Fig. 5) with the following different  
 678 numerical resolutions:  $150 \times 150$ ,  $300 \times 300$ ,  $500 \times 500$ ,  $700 \times 700$  and  $900 \times 900$  grid points (Fig.  
 679 A1). For a dimensionless model time of 950, the ratio of the mean porosity in the model  
 680 domain divided by the mean porosity for a simulation with  $900 \times 900$  grid points is plotted  
 681 versus the corresponding resolution for simulations with different resolution (Fig. A1A).  
 682 Similar ratios are plotted for the minimum fluid pressure in the model domain and the vein  
 683 length. The higher the resolution, the less the three ratios vary, indicating the convergence of  
 684 the numerical results upon increasing numerical resolution. The evolution of the minimum

685 fluid pressure in the model domain with time is shown for different numerical resolutions  
686 (Fig. A1B). With larger numerical resolution, the temporal evolution of the minimum fluid  
687 pressure varies less, indicating again the convergence of the numerical results for increasing  
688 numerical resolution. Finally, the spatial distribution of  $p_f$  at a dimensionless time of 785 is  
689 displayed for three different resolutions (Fig. A1C to E). For a resolution of  $150 \times 150$  the  
690 contours of  $p_f$  are jagged, confirming an insufficient numerical resolution (Fig. A1C). For  
691 numerical resolutions of  $500 \times 500$  and  $900 \times 900$  the contours of  $p_f$  are smooth and the  
692 colormaps of  $p_f$  cannot be distinguished by eye (Fig. A1D and E). The numerical resolution  
693 test shows that the applied numerical model provides results which converge for increasing  
694 numerical resolution and are, hence, not dependent on the numerical resolution.

695

696 **References**

697 Aharonov, E., M. Spiegelman, and P. Kelemen (1997), Three-dimensional flow and reaction  
698 in porous media: Implications for the Earth's mantle and sedimentary basins, *Journal of*  
699 *Geophysical Research-Solid Earth*, 102(B7), 14821-14833, doi:10.1029/97jb00996.

700 Aharonov, E., J. A. Whitehead, P. B. Kelemen, and M. Spiegelman (1995), Channeling  
701 instability of upwelling melt in the mantle, *Journal of Geophysical Research-Solid Earth*,  
702 100(B10), 20433-20450, doi:10.1029/95jb01307.

703 Audet, P., M. G. Bostock, N. I. Christensen, and S. M. Peacock (2009), Seismic evidence for  
704 overpressured subducted oceanic crust and megathrust fault sealing, *Nature*, 457(7225), 76-  
705 78, doi:10.1038/nature07650.

706 Baltzell, C., E. M. Parmentier, Y. Liang, and S. Tirupathi (2015), A high-order numerical  
707 study of reactive dissolution in an upwelling heterogeneous mantle: 2. Effect of shear  
708 deformation, *Geochemistry Geophysics Geosystems*, 16(11), 3855-3869,  
709 doi:10.1002/2015gc006038.

710 Bebout, G. E. (2014), Chemical and Isotopic Cycling in Subduction Zones, in *Treatise on*  
711 *Geochemistry*, edited by H. D. Holland and K. K. Turekian, pp. 703-747, Elsevier.

712 Beinlich, A., T. John, J. Vrijmoed, M. Tominaga, T. Magna, and Y. Podladchikov (2020),  
713 Instantaneous rock transformations in the deep crust driven by reactive fluid flow, *Nature*  
714 *Geoscience*, 13(4), 307-311.

715 Bessat, A., S. Pilet, Y. Y. Podladchikov, and S. M. Schmalholz (2022), Melt Migration and  
716 Chemical Differentiation by Reactive Porosity Waves, *Geochemistry Geophysics*  
717 *Geosystems*, 23(2), doi:10.1029/2021gc009963.

718 Bloch, W., T. John, J. Kummerow, P. Salazar, O. S. Krüger, and S. A. Shapiro (2018),  
719 Watching Dehydration: Seismic Indication for Transient Fluid Pathways in the Oceanic  
720 Mantle of the Subducting Nazca Slab, *Geochemistry, Geophysics, Geosystems*, 19(9), 3189-  
721 3207, doi:<https://doi.org/10.1029/2018GC007703>.

722 Brantut, N., J. Sulem, and A. Schubnel (2011), Effect of dehydration reactions on earthquake  
723 nucleation: Stable sliding, slow transients, and unstable slip, *Journal of Geophysical*  
724 *Research: Solid Earth*, 116(B5).

725 Burlini, L., G. Di Toro, and P. Meredith (2009), Seismic tremor in subduction zones: Rock  
726 physics evidence, *Geophysical Research Letters*, 36, doi:[10.1029/2009gl037735](https://doi.org/10.1029/2009gl037735).

727 Chernak, L. J., and G. Hirth (2010), Deformation of antigorite serpentinite at high temperature  
728 and pressure, *Earth and Planetary Science Letters*, 296(1-2), 23-33,  
729 doi:[10.1016/j.epsl.2010.04.035](https://doi.org/10.1016/j.epsl.2010.04.035).

730 Connolly, J. (1997), Devolatilization-generated fluid pressure and deformation-propagated  
731 fluid flow during prograde regional metamorphism, *Journal of Geophysical Research: Solid*  
732 *Earth*, 102(B8), 18149-18173.

733 Connolly, J. (2005), Computation of phase equilibria by linear programming: a tool for  
734 geodynamic modeling and its application to subduction zone decarbonation, *Earth and*  
735 *Planetary Science Letters*, 236(1-2), 524-541.

736 Connolly, J. (2009), The geodynamic equation of state: What and how, *Geochemistry*  
737 *Geophysics Geosystems*, 10, doi:[10.1029/2009gc002540](https://doi.org/10.1029/2009gc002540).

738 Cruz-Atienza, V. M., C. Villafuerte, and H. S. Bhat (2018), Rapid tremor migration and pore-  
739 pressure waves in subduction zones, *Nature Communications*, 9(1), 2900,  
740 doi:[10.1038/s41467-018-05150-3](https://doi.org/10.1038/s41467-018-05150-3).

741 David, E. C., N. Brantut, L. N. Hansen, and T. M. Mitchell (2018), Absence of Stress-Induced  
742 Anisotropy During Brittle Deformation in Antigorite Serpentinite, *Journal of Geophysical*  
743 *Research-Solid Earth*, 123(12), 10616-10644, doi:10.1029/2018jb016255.

744 Evans, O., M. Spiegelman, and P. B. Kelemen (2020), Phase-Field Modeling of Reaction-  
745 Driven Cracking: Determining Conditions for Extensive Olivine Serpentinization, *Journal of*  
746 *Geophysical Research: Solid Earth*, 125(1), e2019JB018614.

747 Fowler, A. C. (1985), A mathematical model of magma transport in the asthenosphere,  
748 *Geophysical & Astrophysical Fluid Dynamics*, 33(1-4), 63-96,  
749 doi:10.1080/03091928508245423.

750 Frank, W. B., N. M. Shapiro, A. L. Husker, V. Kostoglodov, H. S. Bhat, and M. Carnpillo  
751 (2015), Along-fault pore-pressure evolution during a slow-slip event in Guerrero, Mexico,  
752 *Earth and Planetary Science Letters*, 413, 135-143, doi:10.1016/j.epsl.2014.12.051.

753 Gerya, T. (2019), *Introduction to numerical geodynamic modelling*, Cambridge University  
754 Press.

755 Gomberg, J., Cascadia, and B. W. Group (2010), Slow-slip phenomena in Cascadia from  
756 2007 and beyond: A review, *Bulletin*, 122(7-8), 963-978.

757 Hacker, B. R., S. M. Peacock, G. A. Abers, and S. D. Holloway (2003), Subduction factory 2.  
758 Are intermediate-depth earthquakes in subducting slabs linked to metamorphic dehydration  
759 reactions?, *Journal of Geophysical Research: Solid Earth*, 108(B1).

760 Hatakeyama, K., I. Katayama, K.-i. Hirauchi, and K. Michibayashi (2017), Mantle hydration  
761 along outer-rise faults inferred from serpentinite permeability, *Scientific Reports*, 7(1), 13870,  
762 doi:10.1038/s41598-017-14309-9.

763 Hebert, L. B., P. Antoshechkina, P. Asimow, and M. Gurnis (2009), Emergence of a low-  
764 viscosity channel in subduction zones through the coupling of mantle flow and  
765 thermodynamics, *Earth and Planetary Science Letters*, 278(3-4), 243-256,  
766 doi:10.1016/j.epsl.2008.12.013.

767 Hermann, J., O. Müntener, and M. Scambelluri (2000), The importance of serpentinite  
768 mylonites for subduction and exhumation of oceanic crust, *Tectonophysics*, 327(3-4), 225-  
769 238.

770 Hilairet, N., B. Reynard, Y. B. Wang, I. Daniel, S. Merkel, N. Nishiyama, and S. Petitgirard  
771 (2007), High-pressure creep of serpentine, interseismic deformation, and initiation of  
772 subduction, *Science*, 318(5858), 1910-1913, doi:10.1126/science.1148494.

773 Hirauchi, K., I. Katayama, and Y. Kouketsu (2020), Semi-brittle deformation of antigorite  
774 serpentinite under forearc mantle wedge conditions, *Journal of Structural Geology*, 140,  
775 doi:10.1016/j.jsg.2020.104151.

776 Holland, T., and R. Powell (1998), An internally consistent thermodynamic data set for  
777 phases of petrological interest, *Journal of metamorphic Geology*, 16(3), 309-343.

778 Huber, K., J. C. Vrijmoed, and T. John (2022), Formation of Olivine Veins by Reactive Fluid  
779 Flow in a Dehydrating Serpentinite, *Geochemistry, Geophysics, Geosystems*, 23(6),  
780 e2021GC010267, doi:<https://doi.org/10.1029/2021GC010267>.

781 John, T., N. Gussone, Y. Y. Podladchikov, G. E. Bebout, R. Dohmen, R. Halama, R. Klemd,  
782 T. Magna, and H. M. Seitz (2012), Volcanic arcs fed by rapid pulsed fluid flow through  
783 subducting slabs, *Nature Geoscience*, 5(7), 489-492, doi:10.1038/ngeo1482.

784 Kato, A., et al. (2010), Variations of fluid pressure within the subducting oceanic crust and  
785 slow earthquakes, *Geophysical Research Letters*, 37, doi:10.1029/2010gl043723.

786 Kempf, E. D., J. Hermann, E. Reusser, L. P. Baumgartner, and P. Lanari (2020), The role of  
787 the antigorite + brucite to olivine reaction in subducted serpentinites (Zermatt, Switzerland)  
788 (vol 113, 16, 2020), *Swiss Journal of Geosciences*, 113(1), doi:10.1186/s00015-020-00377-z.

789 Kolditz, O., H. Shao, W. Wang, and S. Bauer (2016), *Thermo-hydro-mechanical chemical*  
790 *processes in fractured porous media: modelling and benchmarking*, 313 pp., Springer,  
791 doi:10.1007/978-3-319-11894-9.

792 Labrousse, L., G. Hetenyi, H. Raimbourg, L. Jolivet, and T. B. Andersen (2010), Initiation of  
793 crustal-scale thrusts triggered by metamorphic reactions at depth: Insights from a comparison  
794 between the Himalayas and Scandinavian Caledonides, *Tectonics*, 29,  
795 doi:10.1029/2009tc002602.

796 Llana-Fúnez, S., J. Wheeler, and D. R. Faulkner (2012), Metamorphic reaction rate controlled  
797 by fluid pressure not confining pressure: implications of dehydration experiments with  
798 gypsum, *Contributions to Mineralogy and Petrology*, 164(1), 69-79, doi:10.1007/s00410-012-  
799 0726-8.

800 Malvoisin, B., Y. Y. Podladchikov, and A. V. Myasnikov (2021), Achieving complete  
801 reaction while the solid volume increases: A numerical model applied to serpentinisation,  
802 *Earth and Planetary Science Letters*, 563, doi:10.1016/j.epsl.2021.116859.

803 Matter, J. M., and P. B. Kelemen (2009), Permanent storage of carbon dioxide in geological  
804 reservoirs by mineral carbonation, *Nature Geoscience*, 2(12), 837-841, doi:10.1038/ngeo683.

805 McKenzie, D. (1984), The generation and compaction of partially molten rock, *J. Petrology*,  
806 25, 713-765.

807 Moulas, E., S. M. Schmalholz, Y. Podladchikov, L. Tajčmanová, D. Kostopoulos, and L.  
808 Baumgartner (2019), Relation between mean stress, thermodynamic, and lithostatic pressure,  
809 *Journal of metamorphic geology*, 37(1), 1-14.

810 Omlin, S., B. Malvoisin, and Y. Y. Podladchikov (2017), Pore fluid extraction by reactive  
811 solitary waves in 3-D, *Geophysical Research Letters*, 44(18), 9267-9275.

812 Pandey, S. N., V. Vishal, and A. Chaudhuri (2018), Geothermal reservoir modeling in a  
813 coupled thermo-hydro-mechanical-chemical approach: A review, *Earth-Science Reviews*,  
814 185, 1157-1169, doi:10.1016/j.earscirev.2018.09.004.

815 Peacock, S. M. (1990), Fluid processes in subduction zones, *Science*, 248(4953), 329-337,  
816 doi:10.1126/science.248.4953.329.

817 Peng, Z. G., and J. Gombert (2010), An integrated perspective of the continuum between  
818 earthquakes and slow-slip phenomena, *Nature Geoscience*, 3(9), 599-607,  
819 doi:10.1038/ngeo940.

820 Peters, D., T. Pettke, T. John, and M. Scambelluri (2020), The role of brucite in water and  
821 element cycling during serpentinite subduction – Insights from Erro Tobbio (Liguria, Italy),  
822 *Lithos*, 360-361, 105431, doi:https://doi.org/10.1016/j.lithos.2020.105431.

823 Pettke, T., and A. Bretscher (2022), Fluid-mediated element cycling in subducted oceanic  
824 lithosphere: The orogenic serpentinite perspective, *Earth-Science Reviews*, 225,  
825 doi:10.1016/j.earscirev.2021.103896.

826 Plümper, O., T. John, Y. Y. Podladchikov, J. C. Vrijmoed, and M. Scambelluri (2017), Fluid  
827 escape from subduction zones controlled by channel-forming reactive porosity, *Nature*  
828 *Geoscience*, 10(2), 150-156.

829 Poulet, T., A. Karrech, K. Regenauer-Lieb, L. Fisher, and P. Schaub (2012), Thermal–  
830 hydraulic–mechanical–chemical coupling with damage mechanics using ESCRIPTRT and  
831 ABAQUS, *Tectonophysics*, 526, 124-132.

832 Poulet, T., M. Veveakis, M. Herwegh, T. Buckingham, and K. Regenauer-Lieb (2014),  
833 Modeling episodic fluid-release events in the ductile carbonates of the Glarus thrust,  
834 *Geophysical Research Letters*, 41(20), 7121-7128, doi:10.1002/2014gl061715.

835 Rass, L., D. Kolyukhin, and A. Minakov (2019), Efficient parallel random field generator for  
836 large 3-D geophysical problems, *Computers & Geosciences*, 131, 158-169,  
837 doi:10.1016/j.cageo.2019.06.007.

838 Reiner, M. (1964), The Deborah number, *Physics Today*, 17(1), 62.

839 Rupke, L. H., J. P. Morgan, M. Hort, and J. A. D. Connolly (2004), Serpentine and the  
840 subduction zone water cycle, *Earth and Planetary Science Letters*, 223(1-2), 17-34,  
841 doi:10.1016/j.epsl.2004.04.018.

842 Scambelluri, M., J. Fiebig, N. Malaspina, O. Muntener, and T. Pettke (2004), Serpentinite  
843 subduction: Implications for fluid processes and trace-element recycling, *International*  
844 *Geology Review*, 46(7), 595-613, doi:10.2747/0020-6814.46.7.595.

845 Scambelluri, M., O. Muntener, J. Hermann, G. B. Piccardo, and V. Trommsdorff (1995),  
846 Subduction of water into the mantle - history of an Alpine peridotite, *Geology*, 23(5), 459-  
847 462, doi:10.1130/0091-7613(1995)023<0459:Sowitm>2.3.Co;2.

848 Scambelluri, M., E. H. H. Strating, G. B. Piccardo, R. L. M. Vissers, and E. Rampone (1991),  
849 Alpine olivine-bearing and titanium clinohumite-bearing assemblages in the Erro Tobbio  
850 peridotite (Voltri-massif, NW Italy), *Journal of Metamorphic Geology*, 9(1), 79-91,  
851 doi:10.1111/j.1525-1314.1991.tb00505.x.

852 Schiemenz, A., Y. Liang, and E. M. Parmentier (2011), A high-order numerical study of  
853 reactive dissolution in an upwelling heterogeneous mantle-I. Channelization, channel  
854 lithology and channel geometry, *Geophysical Journal International*, 186(2), 641-664,  
855 doi:10.1111/j.1365-246X.2011.05065.x.

856 Schmalholz, S. M., E. Moulas, O. Plumper, A. V. Myasnikov, and Y. Y. Podladchikov  
857 (2020), 2D Hydro-Mechanical-Chemical Modeling of (De)hydration Reactions in Deforming  
858 Heterogeneous Rock: The Periclase-Brucite Model Reaction, *Geochemistry Geophysics  
859 Geosystems*, 21(11), doi:10.1029/2020gc009351.

860 Schmalholz, S. M., and L. Räss (2022), PTsolvers/PseudoTransientHMC.jl:  
861 PseudoTransientHMC.jl 0.1.0 (v0.1.0), edited, Zenodo,  
862 doi:<https://doi.org/10.5281/zenodo.6559431>.

863 Schmeling, H., J. P. Kruse, and G. Richard (2012), Effective shear and bulk viscosity of  
864 partially molten rock based on elastic moduli theory of a fluid filled poroelastic medium,  
865 *Geophysical Journal International*, 190(3), 1571-1578, doi:10.1111/j.1365-  
866 246X.2012.05596.x.

867 Shelly, D. R., G. C. Beroza, and S. Ide (2007), Non-volcanic tremor and low-frequency  
868 earthquake swarms, *Nature*, 446(7133), 305-307.

869 Spitz, R., S. M. Schmalholz, B. J. Kaus, and A. A. Popov (2020), Quantification and  
870 visualization of finite strain in 3D viscous numerical models of folding and overthrusting,  
871 *Journal of Structural Geology*, 131, 103945.

872 Sulem, J., and V. Famin (2009), Thermal decomposition of carbonates in fault zones: Slip-  
873 weakening and temperature-limiting effects, *Journal of Geophysical Research: Solid Earth*,  
874 114(B3).

875 Taetz, S., T. John, M. Brocker, C. Spandler, and A. Stracke (2018), Fast intraslab fluid-flow  
876 events linked to pulses of high pore fluid pressure at the subducted plate interface, *Earth and*  
877 *Planetary Science Letters*, 482, 33-43, doi:10.1016/j.epsl.2017.10.044.

878 Tarling, M. S., S. A. F. Smith, and J. M. Scott (2019), Fluid overpressure from chemical  
879 reactions in serpentinite within the source region of deep episodic tremor, *Nature Geoscience*,  
880 12(12), 1034-1042, doi:10.1038/s41561-019-0470-z.

881 Ulmer, P., and V. Trommsdorff (1995), Serpentine Stability to Mantle Depths and  
882 Subduction-Related Magmatism, *Science*, 268(5212), 858-861,  
883 doi:doi:10.1126/science.268.5212.858.

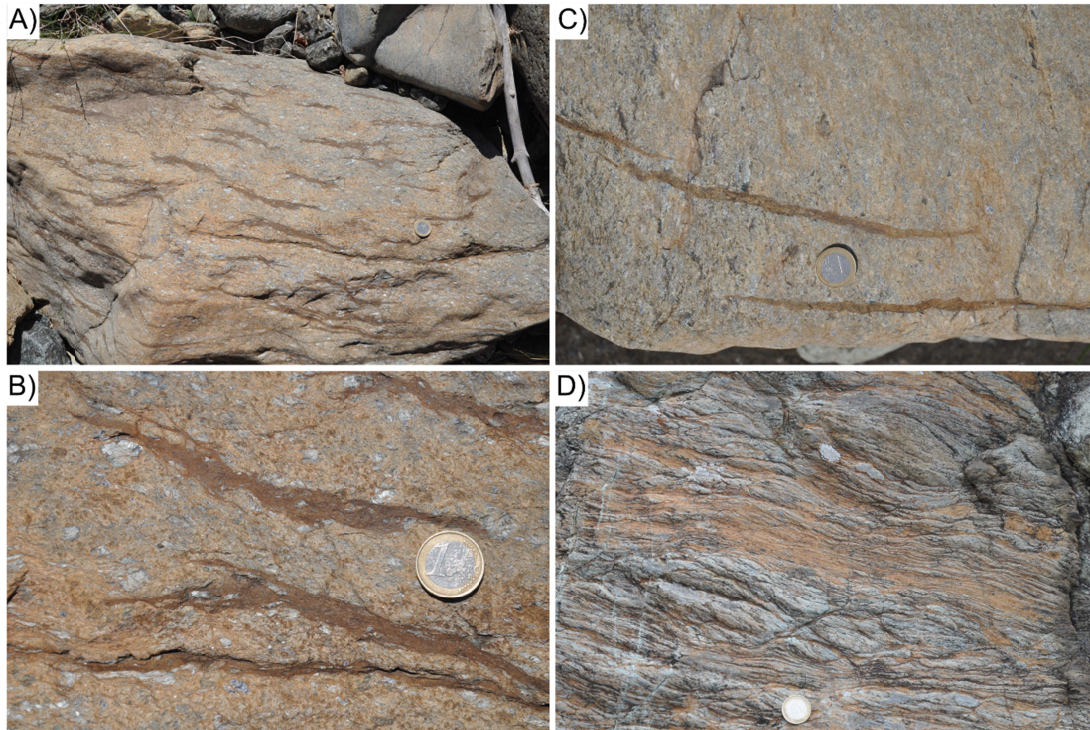
884 Van Avendonk, H. J. A., W. S. Holbrook, D. Lizarralde, M. M. Mora, S. Harder, A. D.  
885 Bullock, G. E. Alvarado, and C. J. Ramirez (2010), Seismic evidence for fluids in fault zones  
886 on top of the subducting Cocos Plate beneath Costa Rica, *Geophysical Journal International*,  
887 181(2), 997-1016, doi:10.1111/j.1365-246X.2010.04552.x.

888 Wang, L. H., V. M. Yarushina, Y. Alkhimenkov, and Y. Podladchikov (2021), Physics-  
889 inspired pseudo-transient method and its application in modelling focused fluid flow with  
890 geological complexity, *Geophysical Journal International*, 229(1), 1-20,  
891 doi:10.1093/gji/ggab426.

892 Yarushina, V. M., and Y. Y. Podladchikov (2015), (De) compaction of porous  
893 viscoelastoplastic media: Model formulation, *Journal of Geophysical Research: Solid Earth*,  
894 120(6), 4146-4170.

895 **Figures with captions**

896

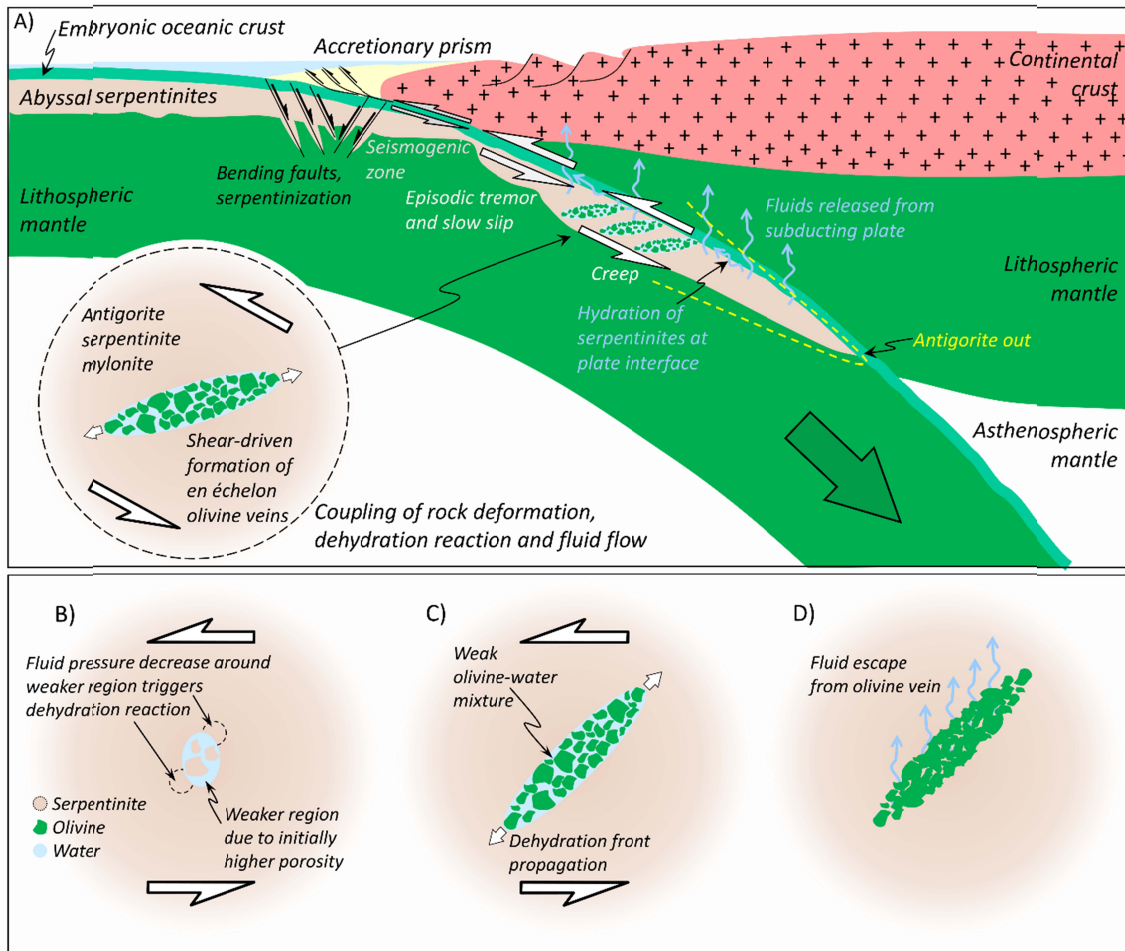


897

898 Figure 1. Natural examples of metamorphic olivine veins in antigorite serpentinite from the  
899 Erro Tobbio ultramafic rocks, Ligurian Alps, Italy. A) Overview on the limited spatial extent  
900 of olivine bearing veins (with darker color) in weakly deformed serpentinitized peridotite. Coin  
901 diameter is 2.4 cm. B) Olivine veins with characteristic spacing and aspect ratios in  
902 serpentinitised peridotite. Detail of picture in A). C) olivine-bearing veins in a serpentinitised  
903 peridotite, foliation is sub vertical, extent of veins is ca. 20 cm. D) Serpentinite mylonite with  
904 different generations of olivine veins. An earlier set is subparallel to the foliation, younger  
905 shear bands dissect serpentinite mylonite and olivine veins. Top-to-the-left shear sense. Note  
906 the late stage serpentine veins perpendicular to the foliation.

907

908

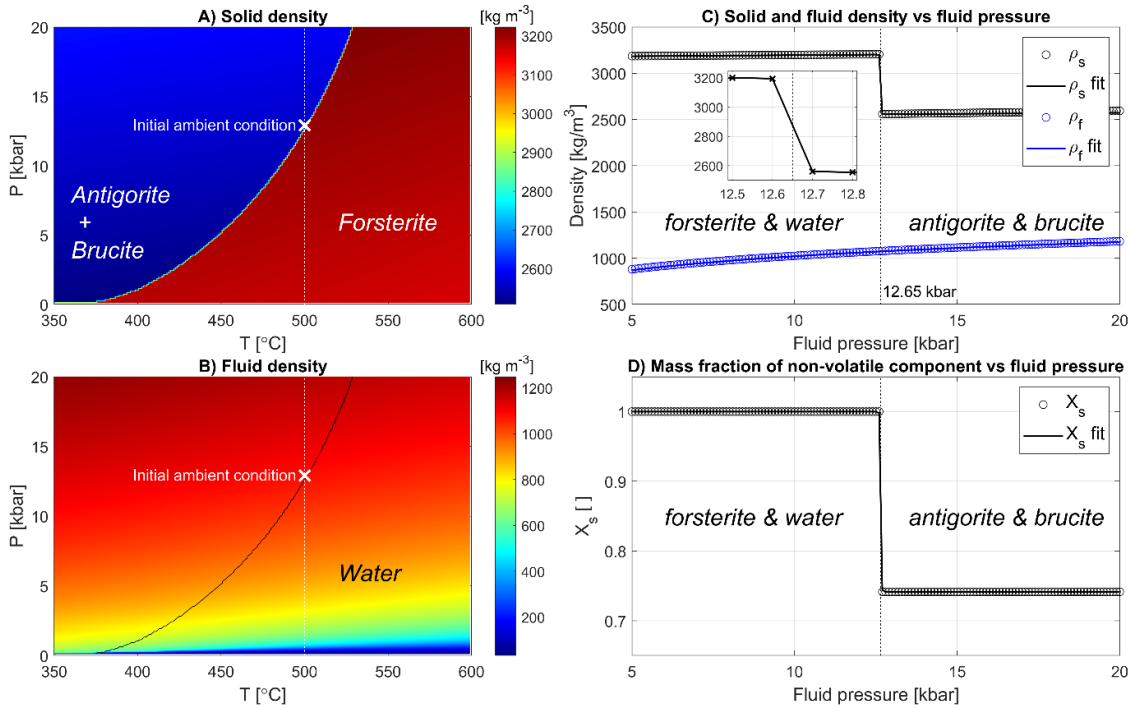


909

910 Figure 2. Simple sketches illustrating the geodynamic setting (A) and the hypothesis for  
911 shear-driven dehydration and olivine vein formation in viscous serpentinite (B to D; see text  
912 for details).

913

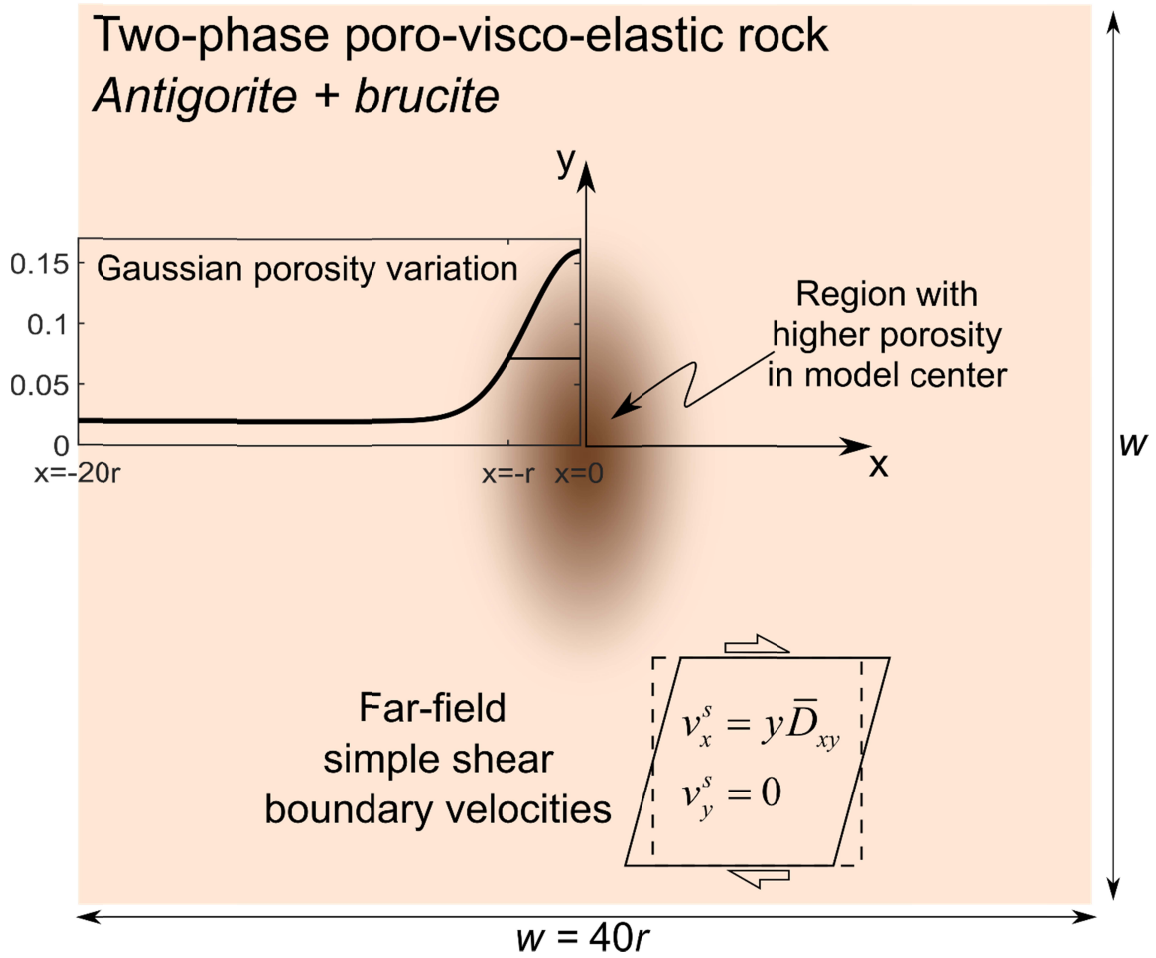
914



915

916 Figure 3. Thermodynamic results obtained from Gibbs' free energy minimization for the  
 917 system antigorite + brucite = forsterite + water (see text for exact chemical formulas). Density  
 918 fields of solid (A) and fluid (B) in thermodynamic pressure,  $P$ , and temperature,  $T$ , space.  
 919 Corresponding profiles of solid and fluid densities (C) and mass fraction of MgO (D) as a  
 920 function of fluid pressure at  $500^{\circ}\text{C}$ . The circles in the three profiles in panels C) and D) are  
 921 the results from Gibbs energy minimization and the corresponding solid lines are analytical  
 922 approximations of these profiles (equation (16)), which are used in the numerical algorithm.

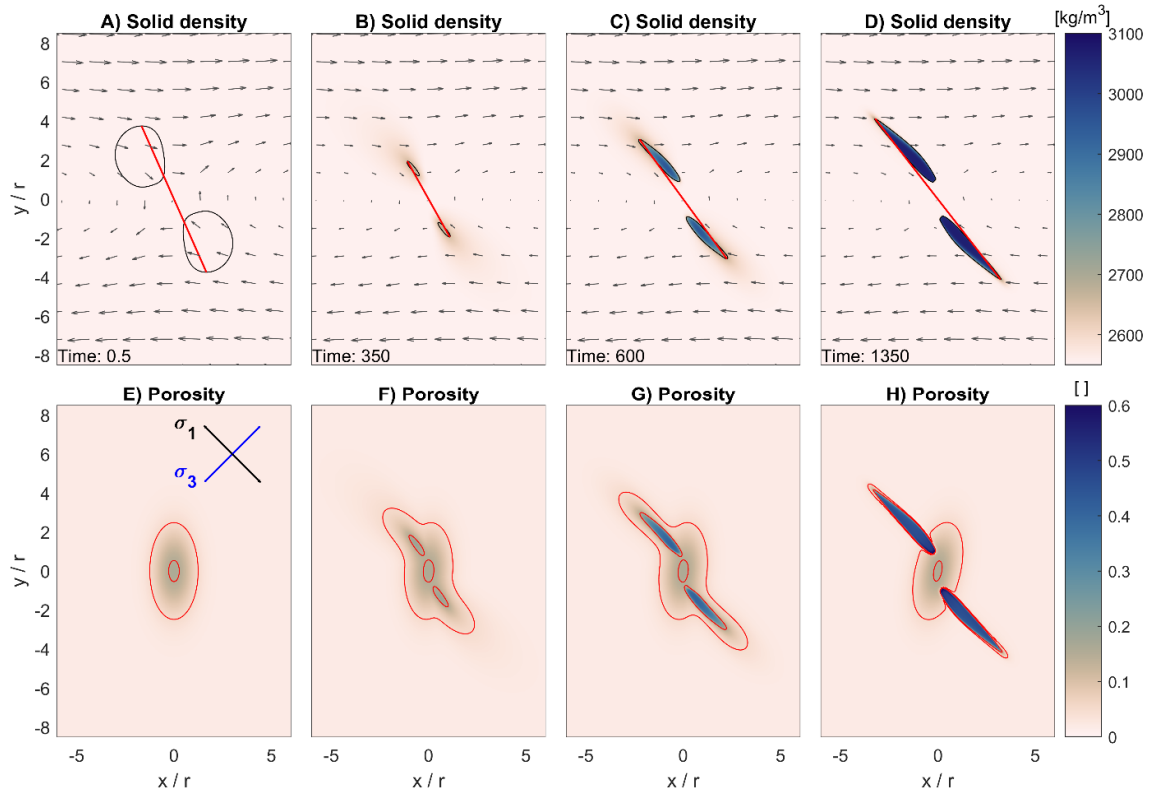
923



924

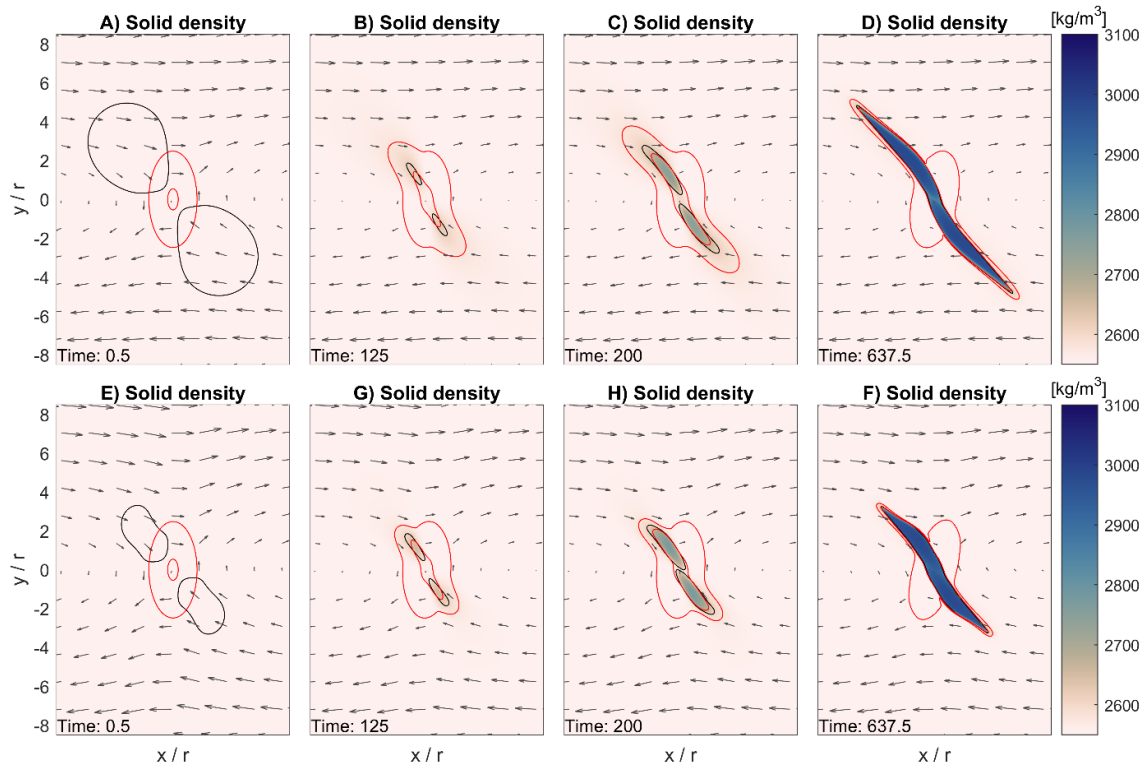
925 Figure 4. Sketch of the model configuration and the applied far-field simple shear (bottom  
 926 right sketch; see text for details). The initial distribution of the porosity is described by a 2D  
 927 Gaussian distribution, having an initial horizontal bandwidth of  $2r$  (graph in left middle of  
 928 the sketch) and a vertical bandwidth of  $4r$ . The width and height of the model is  $40r$  and the  
 929 applied far-field shearing rate is  $\bar{D}_{xy}$ .

930



931

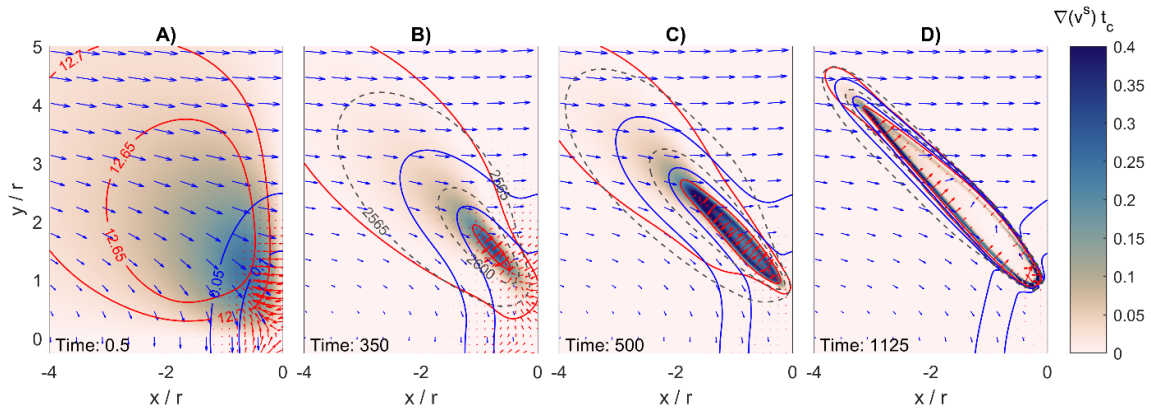
932 Figure 5. Representative evolution of a dehydration vein under simple shear for a simulation  
 933 with  $t_{def}/t_{dif} = 0.071$  and  $t_{kin}/t_{dif} = 0.0025$ . Panels A) to D) show snapshots of solid density  
 934 for four stages of the simulation, indicated by a dimensionless time (see text). The black  
 935 contour lines in panels A) to D) indicated the contour for  $p_f = 12.65$  kbar ( $p_f$  is smaller  
 936 inside the contour), which is the thermodynamic pressure at the dehydration reaction (see Fig.  
 937 3). Grey arrows indicate the solid velocities which are dominated by the applied simple shear.  
 938 The red line connects the highest with the lowest point of the fluid pressure contours and the  
 939 length of the red line is used as proxy to monitor the vein growth with time. Panels E) to H)  
 940 show the porosity corresponding to the model times of panels A) to D). In panel E), the black  
 941 line indicates the direction of the maximal principal stress,  $\sigma_1$ , and the blue line indicates the  
 942 direction of the minimal principal stress,  $\sigma_3$ , at the location of the intersection of the two  
 943 lines. The red contours indicate a porosity of 5% (outer contour) and 15% (inner contour).



945

946 Figure 6. Representative evolution of dehydration veins under simple shear for two  
 947 simulations with  $t_{def} / t_{dif} = 0.038$  and  $t_{kin} / t_{dif} = 0.0025$ . Colomaps indicate the solid density.  
 948 The simulation shown in panels A) to D) is purely viscous whereas for the simulation shown  
 949 in E) to F) a von Mises yield stress of 150 MPa was applied and deformation is visco-plastic.  
 950 In all panels, the black contour lines indicate the contour for  $p_f = 12.65$  kbar ( $p_f$  is smaller  
 951 inside the contour), the grey arrows indicate the solid velocities and the red contours indicate  
 952 a porosity of 5% (outer contour) and 15% (inner contour).

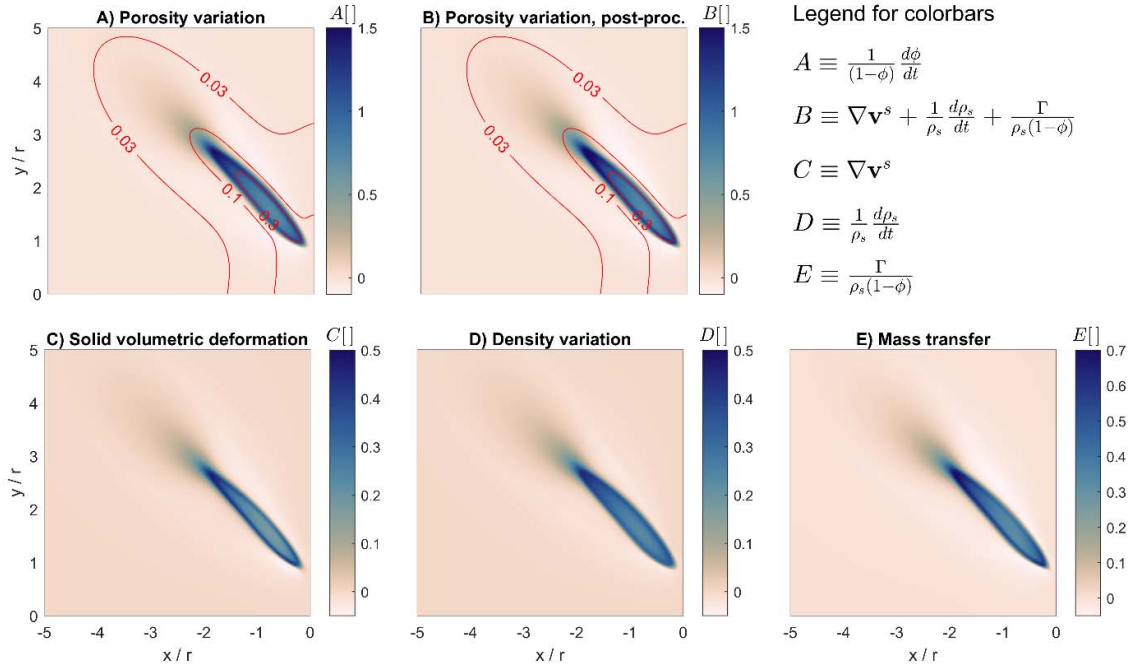
953



954

955 Figure 7. Evolution of a dehydration vein under simple shear for a simulation (shown in Fig.  
 956 5) with  $t_{def} / t_{dif} = 0.071$  and  $t_{kin} / t_{dif} = 0.0025$  at four dimensionless times (see text). The  
 957 colormaps show the dimensionless divergence of the solid velocity, the red arrows show the  
 958 fluid velocity field and the blue arrows show the solid velocity field. The two red contours  
 959 indicate  $p_f = 12.65$  (always the inner contour) and 12.7 kbar. The two blue contours indicate  
 960 a porosity of 5% (outer contour) and 10% (inner contour). The two dashed grey contours  
 961 indicate a solid density of  $2565 \text{ kg/m}^3$  (outer contour) and  $2600 \text{ kg/m}^3$  (inner contour). There  
 962 are no solid density contours in panel A) because all densities are  $< 2565 \text{ kg/m}^3$ .

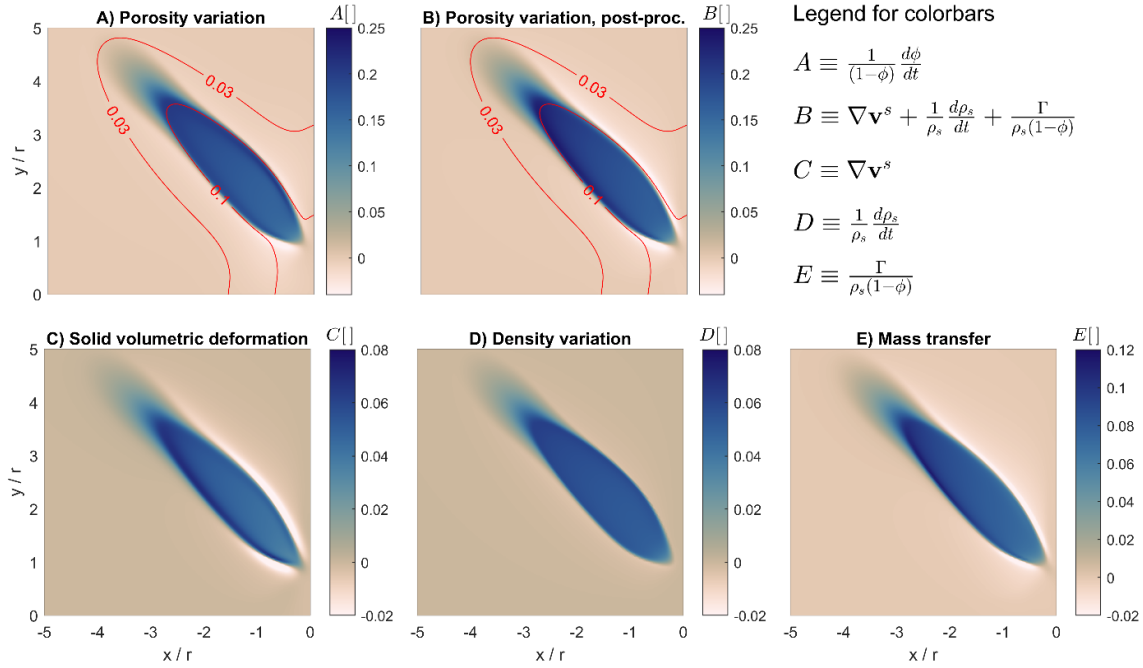
963



964

965 Figure 8. The three mechanisms (solid volumetric deformation, C, solid-density variation, D,  
 966 and mass transfer, E) that control the temporal porosity variation (see equation (18)) for a  
 967 simulation (shown in Fig. 5) with  $t_{def}/t_{dif} = 0.071$  and  $t_{kin}/t_{dif} = 0.0025$  at a dimensionless  
 968 time of 550. A) shows the colormap of the term displayed in the legend for A, B) shows the  
 969 colormap of the term displayed in the legend for B, C) shows the colormap of the term  
 970 displayed in the legend for C, D) shows the colormap of the term displayed in the legend for  
 971 D and E) shows the colormap of the term displayed in the legend for E. All displayed terms  
 972 represent dimensionless rates which can be made dimensionless by multiplying with the  
 973 characteristic time,  $t_c$  (see text).

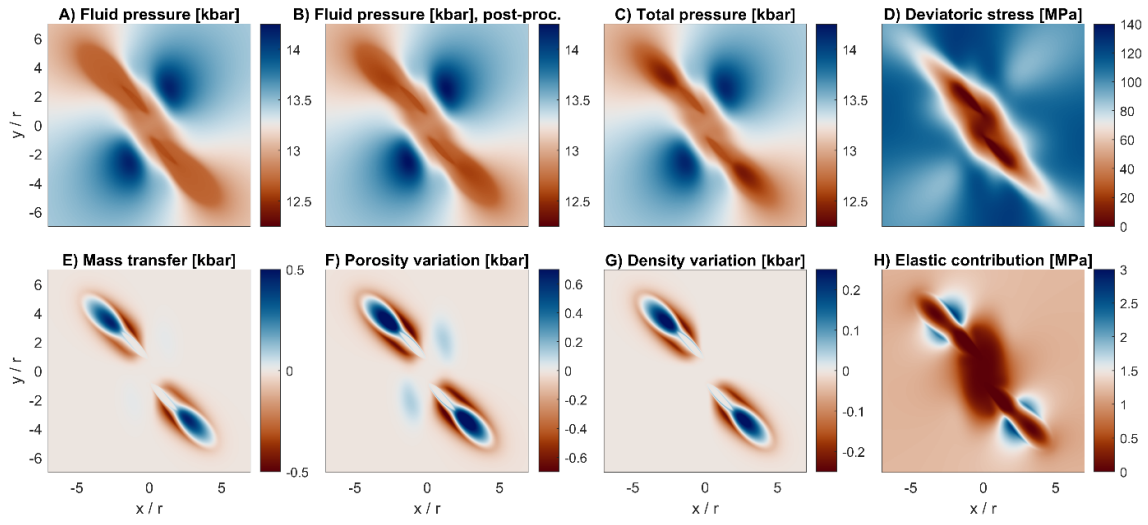
974



975

976 Figure 9. The three mechanisms (solid volumetric deformation, C, solid-density variation, D,  
 977 and mass transfer, E) that control temporal porosity variation (see equation (18)) for a  
 978 simulation with  $t_{def} / t_{dif} = 0.071$  and  $t_{kin} / t_{dif} = 0.022$  at a dimensionless time of 800. A)  
 979 shows the colormap of the term displayed in the legend for A, B) shows the colormap of the  
 980 term displayed in the legend for B, C) shows the colormap of the term displayed in the legend  
 981 for C, D) shows the colormap of the term displayed in the legend for D and E) shows the  
 982 colormap of the term displayed in the legend for E. All displayed terms represent  
 983 dimensionless rates which can be made dimensionless by multiplying with the characteristic  
 984 time,  $t_c$  (see text).

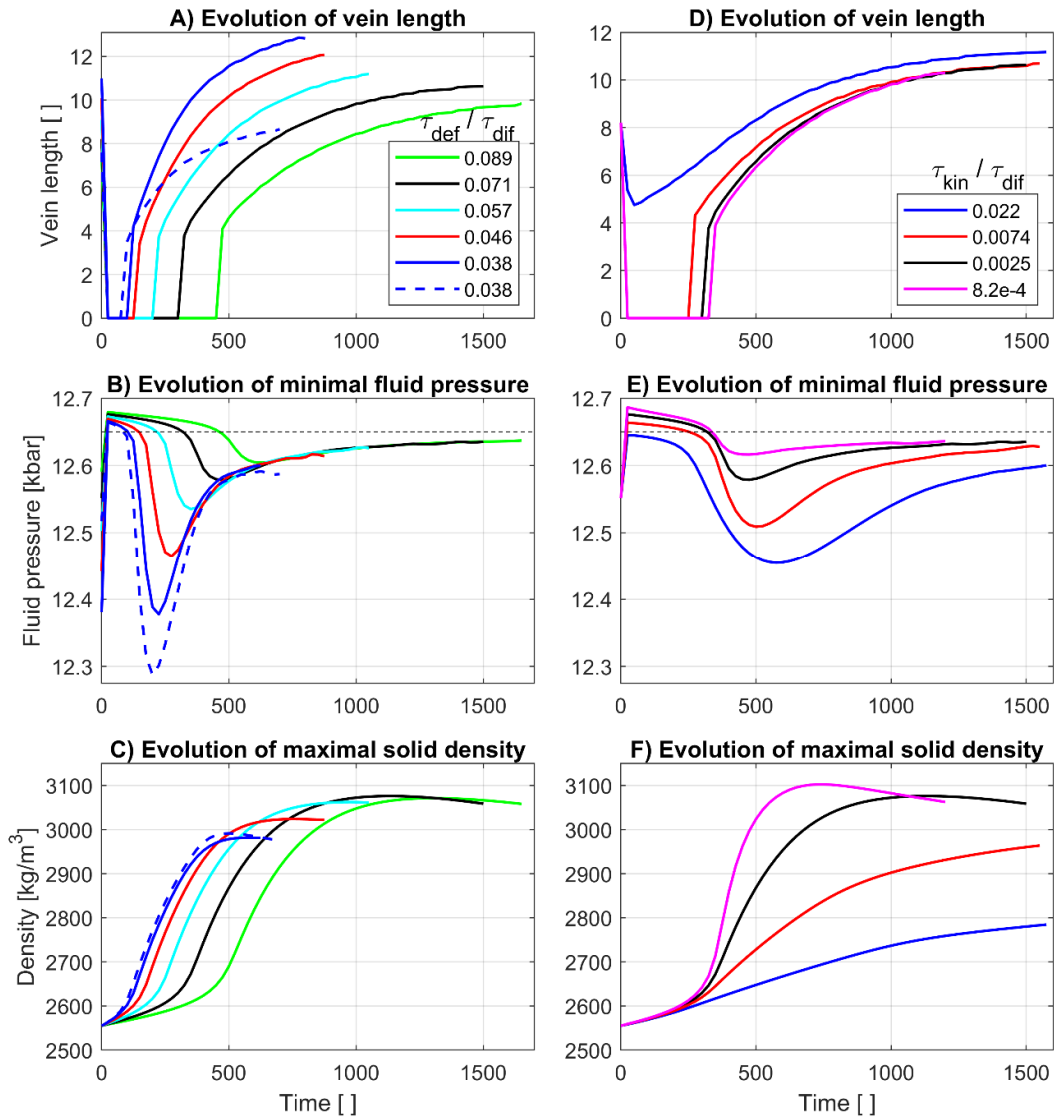
985



986

987 Figure 10. The five mechanisms and quantities that control the distribution of fluid pressure  
988 (equation (19)) for a simulation (shown in Fig. 5) with  $t_{def} / t_{dif} = 0.071$  and  $t_{kin} / t_{dif} = 0.0025$   
989 at a dimensionless time of 550. A) Colormap of fluid pressure which was calculated by the  
990 numerical simulation and B) fluid pressure which was post-processed from numerical results  
991 using equation (19). C) shows the total pressure and D) the deviatoric stress,  $\tau_{II}$ , which was  
992 calculated by the numerical simulation. E) shows the contribution to the fluid pressure due to  
993 mass transfer (last term on right-hand side of equation (19)), F) due to porosity variation  
994 (third term on right-hand side of equation (19)), G) due to solid density variation (fourth term  
995 on right-hand side of equation (19)) and H) due to elastic deformation (second term on right-  
996 hand side of equation (19)). All quantities displayed in E) to H) have been post-processed  
997 from numerical results.

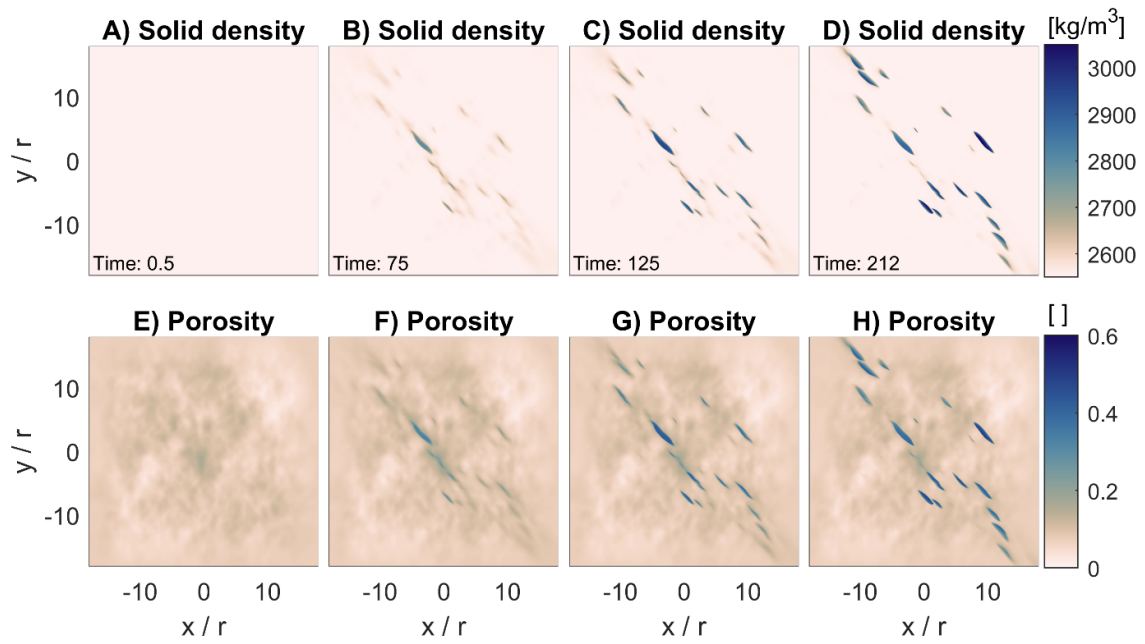
998



999

1000 Figure 11. Impact of far-field shearing rate (A to C) and kinetic reaction rate (B to F) on the  
 1001 evolution of vein length (A and D), on the minimal value of the fluid pressure in the model  
 1002 domain (B and E) and on the evolution of the maximal solid density in the model domain (C  
 1003 and F). For the results displayed in panels A) to C) the ratio  $t_{kin} / t_{dif} = 0.0025$  for all  
 1004 simulations. For the results displayed in panels D) to F) the ratio  $t_{def} / t_{dif} = 0.071$  for all  
 1005 simulations. Results indicated with the dashed blue line are obtained by the same simulation  
 1006 which provided results indicated by the solid blue line, but with a von Mises yield stress of  
 1007 150 MPa (results of the two simulations are also displayed in Fig. 6).

1008



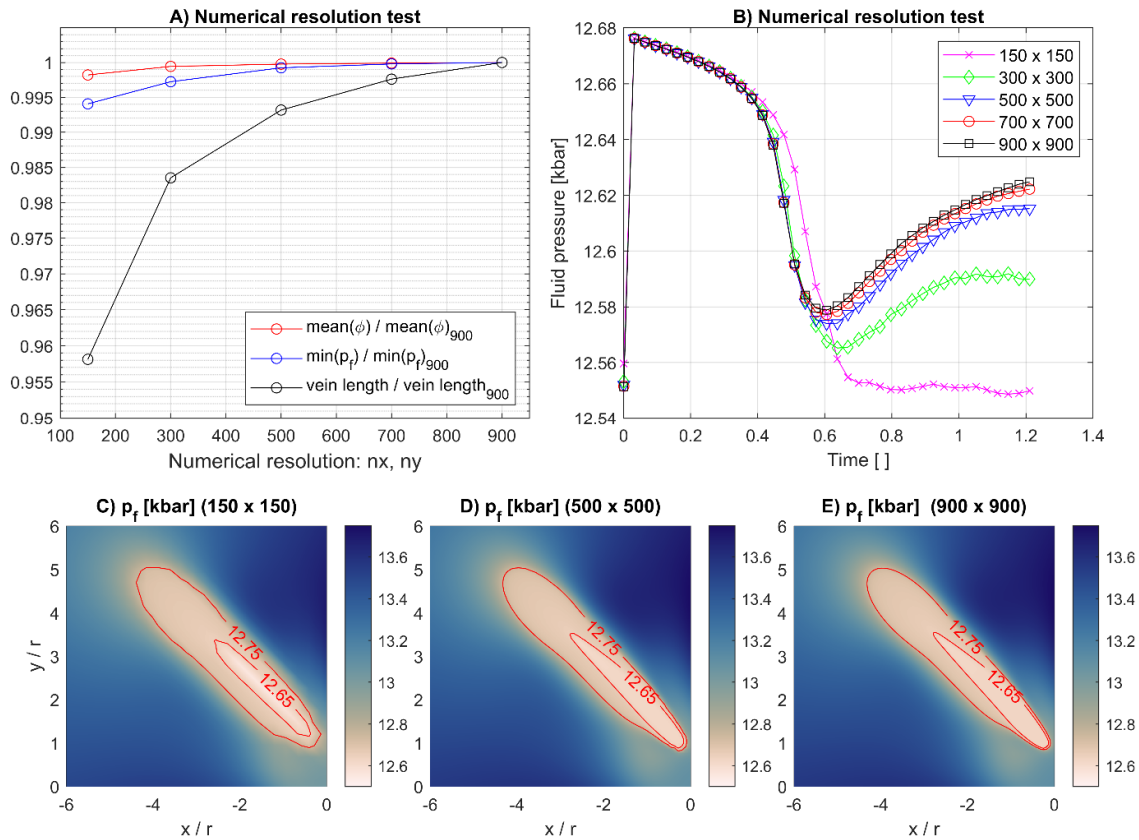
1009

1010 Figure 12. Evolution of solid density (A to D) and corresponding porosity (E to H) for a  
1011 simulation with an initial random distribution of porosity (see Discussion).

1012

1013

1014



1015

1016 Figure A1. Numerical resolution test for the simulation with  $t_{def} / t_{dif} = 0.071$  and  $t_{kin} / t_{dif} =$   
 1017 0.0025 (see Fig. 5). A) For a dimensionless model time of 1.21, the ratio of the mean porosity  
 1018 in the model domain divided by the mean porosity for a simulation with a resolution of  $900 \times$   
 1019  $900$  grid points is plotted versus the corresponding resolution for simulations with different  
 1020 resolution. Similar ratios are plotted for the minimum fluid pressure in the model domain and  
 1021 the vein length. The larger the resolution, the less the three ratios vary. B) Evolution of  
 1022 minimum fluid pressure in the model domain with time for different numerical resolutions  
 1023 (see legend). With larger resolution, the evolution of fluid pressure varies less. C) to D) At a  
 1024 dimensionless model time of 1.0, the colormap of the fluid pressure is displayed for three  
 1025 different resolutions (see numbers in panel titles). Two contour lines of fluid pressure are  
 1026 displayed for better comparability.

1027

1028 Table 1. Model variables and parameters.

Symbol	Name / Definition	Units
$t_{kin}$	Kinetic time scale	[s]
$t_{df}$	$= r^2 \eta_f / (k \varphi_0^3 K_s)$	[s]
$t_{def}$	$= 1 / \bar{D}_{xx}$	[s]
$p_f$	Fluid pressure	[Pa]
$\varphi$	Porosity	[ ]
$\varphi_0$	Initial porosity	[ ]
$\rho_s$	Solid density	[kg · m <sup>-3</sup> ]
$\rho_f$	Fluid density	[kg · m <sup>-3</sup> ]
$X_s$	Mass fraction MgO	[ ]
$p$	Total pressure	[Pa]
$v_x^s, v_y^s$	Solid velocities	[m · s <sup>-1</sup> ]
$v_x^f, v_y^f$	Fluid velocities	[m · s <sup>-1</sup> ]
$ \mathbf{v}^f $	$= \sqrt{(v_x^f)^2 + (v_y^f)^2}$	[m · s <sup>-1</sup> ]
$\tau_{xx}, \tau_{yy}, \tau_{xy}$	Deviatoric stresses	[Pa]
$\tau_{II}$	$= \sqrt{\tau_{xx}^2 + \tau_{xy}^2}$	[Pa]
$k$	Permeability	[m <sup>2</sup> ]
$\eta_f$	Fluid viscosity	[Pa · s]
$\eta_s$	Shear viscosity solid	[Pa · s]
$\lambda$	Bulk viscosity solid	[Pa · s]
$K_s$	Bulk modulus solid	[Pa]
$K_d$	Bulk modulus drained	[Pa]
$p_{ini}$	Initial ambient pressure	[Pa]
$\bar{D}_{xx}$	Far-field deformation rate	[s <sup>-1</sup> ]
$r$	Bandwidth of Gaussian	[m]
$w$	Model width	[m]

1029